

# Investigating Cepheid $\ell$ Carinae’s Cycle-to-cycle Variations via Contemporaneous Velocimetry and Interferometry<sup>★</sup>

R. I. Anderson,<sup>1,2†</sup> A. Mérand,<sup>3</sup> P. Kervella,<sup>4,5</sup> J. Breitsfelder,<sup>3,4</sup> J.-B. LeBouquin,<sup>6</sup> L. Eyer,<sup>7</sup> A. Gallenne,<sup>8</sup> L. Palaversa,<sup>7</sup> T. Semaan,<sup>7</sup> S. Saesen,<sup>7</sup> and N. Mowlavi<sup>7</sup>

<sup>1</sup> Physics and Astronomy Department, The Johns Hopkins University, 3400 N. Charles St, Baltimore, MD 21218, USA

<sup>2</sup> Swiss National Science Foundation Fellow

<sup>3</sup> European Southern Observatory, Alonso de Córdova 3107, Casilla 19001, Santiago 19, Chile

<sup>4</sup> LESIA (UMR 8109), Observatoire de Paris, PSL, CNRS, UPMC, Univ. Paris-Diderot, 5 pl. Jules Janssen, 92195 Meudon, France

<sup>5</sup> Unidad Mixta Internacional Franco-Chilena de Astronomía (UMI 3386), CNRS/INSU, France and

Departamento de Astronomía, Universidad de Chile, Camino El Observatorio 1515, Las Condes, Santiago, Chile

<sup>6</sup> UJF-Grenoble 1 / CNRS-INSU, Institut de Planétologie et d’Astrophysique de Grenoble (IPAG) UMR 5274, F-38041 Grenoble, France

<sup>7</sup> Observatoire de Genève, Université de Genève, 51 Ch. des Maillettes, 1290 Versoix, Switzerland

<sup>8</sup> Departamento de Astronomía, Universidad de Concepción, Casilla 160-C, Concepción, Chile

Accepted 2015 October 17. Received 2015 October 16; in original form 2015 September 21

## ABSTRACT

Baade-Wesselink-type (BW) techniques enable geometric distance measurements of Cepheid variable stars in the Galaxy and the Magellanic clouds. The leading uncertainties involved concern projection factors required to translate observed radial velocities (RVs) to pulsational velocities and recently discovered modulated variability.

We carried out an unprecedented observational campaign involving long-baseline interferometry (VLTI/*PIONIER*) and spectroscopy (Euler/*Coralie*) to search for modulated variability in the long-period ( $P \sim 35.5$  d) Cepheid  $\ell$  Carinae. We determine highly precise angular diameters from squared visibilities and investigate possible differences between two consecutive maximal diameters,  $\Delta_{\max}\Theta$ . We characterize the modulated variability along the line-of-sight using 360 high-precision RVs.

Here we report tentative evidence for modulated angular variability and confirm cycle-to-cycle differences of  $\ell$  Carinae’s RV variability. Two successive maxima yield  $\Delta_{\max}\Theta = 13.1 \pm 0.7(\text{stat.}) \mu\text{as}$  for uniform disk models and  $22.5 \pm 1.4(\text{stat.}) \mu\text{as}$  (4% of the total angular variation) for limb darkened models. By comparing new RVs with 2014 RVs we show modulation to vary in strength. Barring confirmation, our results suggest the optical continuum (traced by interferometry) to be differently affected by modulation than gas motions (traced by spectroscopy). This implies a previously unknown time-dependence of projection factors, which can vary by 5% between consecutive cycles of expansion and contraction.

Additional interferometric data are required to confirm modulated angular diameter variations. By understanding the origin of modulated variability and monitoring its long-term behavior, we aim to improve the accuracy of BW distances and further the understanding of stellar pulsations.

**Key words:** techniques: radial velocities; techniques: high angular resolution; stars: oscillations; stars: variables: Cepheids; stars: individual:  $\ell$  Carinae = HD 84810; distance scale

## 1 INTRODUCTION

Classical Cepheid variable stars are excellent probes of stellar evolution and pulsation physics. Moreover, they are crucial calibrators of cosmic distances and hold the key for determining the Hubble constant to within a couple of percent accuracy (e.g. [Riess et al. 2011](#); [Freedman et al. 2012](#)), aiding in the interpretation of the cos-

<sup>★</sup> Based on observations collected with *PIONIER* at the ESO Very Large Telescope Interferometer located at ESO Paranal Observatory under programme number 094.D-0584 and on observations collected with the *Coralie* echelle spectrograph mounted to the Swiss 1.2m Euler telescope located at La Silla Observatory, Chile.

<sup>†</sup> E-mail: [ria@jhu.edu](mailto:ria@jhu.edu)

mic microwave background for cosmology. (Hinshaw et al. 2013; Planck Collaboration et al. 2014)

Large efforts are currently under way to push the accuracy of a measurement of the local Hubble constant,  $H_0$ , to 1% (Suyu et al. 2012). Improved Cepheid distances are a crucial element in pursuit of such extreme cosmological precision. Extragalactic Cepheid distances are typically determined using period-luminosity relations (PLRs, Leavitt 1908; Leavitt & Pickering 1912) whose calibration is achieved more locally, e.g. in the Galaxy (Feast & Catchpole 1997; van Leeuwen et al. 2007; Benedict et al. 2007), the Large Magellanic Cloud (e.g. Soszynski et al. 2008; Groenewegen 2013; Macri et al. 2015), the mega-maser galaxy NGC 4258 (Macri et al. 2006; Humphreys et al. 2013; Hoffmann & Macri 2015), or combinations of these (e.g. Riess et al. 2011). One remaining key issue in this context is how chemical composition affects the calibration of PLRs.

An investigation into the impact of metallicity on slope and zero-point of PLRs requires distance measurements to individual Cepheids of different metallicities. While ESA’s space mission *Gaia* will soon provide an unprecedented data set of extremely accurate Cepheid parallaxes, the metallicity range spanned by this sample will be relatively small. Extending the sample to Cepheids in the Magellanic clouds would provide a stronger handle on metallicity. However, even *Gaia* will not be able to measure individual Cepheid parallaxes at such great distances with the accuracy required to separate depth effects inside the LMC from metallicity effects on PLRs. This point is particularly difficult for the Small Magellanic Cloud (Scowcroft et al. 2015), which provides the greatest lever for metallicity.

Fortunately, variants of the Baade-(Becker-)Wesselink (BW; Lindemann 1918; Baade 1926; Becker 1940; Wesselink 1946) technique afford a homogeneous methodology for determining individual geometric distances to Cepheids in the Galaxy, LMC, and SMC (e.g. Storm et al. 2004; Groenewegen 2008; Storm et al. 2011; Groenewegen 2013). However, BW distances have suffered from systematic difficulties related to the calibration of the projection factor as described below. This has limited their ability to reveal how metallicity affects the PLR. It is therefore important to improve the accuracy of BW distances, and new observational opportunities such as long-baseline near-infrared (NIR) interferometry (e.g. Fouqué & Gieren 1997; Nordgren et al. 2000; Kervella et al. 2001, 2004a,b) and infrared surface brightness relations (Kervella et al. 2004c) are providing ever higher precision.

BW techniques exploit pulsational motion to measure *geometric* distances. In essence, distance

$$d [\text{pc}] = 9.3095 \cdot \Delta R [R_\odot] / \Delta \Theta [\text{mas}], \quad (1)$$

where  $\Delta R$  denotes the *linear* radius variation in  $R_\odot$  (using  $R_\odot = 696,342 \pm 65$  km from Emilio et al. 2012) as measured from radial velocities (RVs) and  $\Delta \Theta$  the angular diameter variation in *milliarcseconds*. The method’s accuracy rests to a large extent on the empirically calibrated projection factor  $p$  (see Breitfelder et al., in preparation), since  $p$  is required to translate observed line-of-sight velocities (which integrate over a limb-darkened disk) to the pulsational velocity as seen from the star’s center. The linear equivalent to  $\Delta \Theta$  is thus obtained by computing

$$\Delta R = p \cdot \int_{t_1}^{t_2} v_r dt. \quad (2)$$

Nardetto et al. (2007) decomposed this projection factor as

$$p = p_o f_{\text{grad}} f_{o-g}, \quad (3)$$

where geometric aspects of limb darkening and disk integration are included in  $p_o$ , velocity differences between the *optical* and *gas* photospheric layers are represented by  $f_{o-g}$ , and velocity gradients acting over the line forming region by  $f_{\text{grad}}$ .

Sabbey et al. (1995) and Nardetto et al. (2004) investigated how the characteristic, variable spectral line asymmetry of Cepheids introduces a (repeating) phase-dependence of projection factors. It is generally assumed, however, that these variations of  $p$  cancel out when integrating over an entire pulsation cycle.

Recently, Anderson (2014) demonstrated an additional difficulty for determining BW distances. Four Cepheids were shown to exhibit modulated RV curves, where modulation refers to differences in RV curve shape that occur on time-scales from weeks to years. RV curve modulation can lead to significant differences in

$$\Delta R/p = \int_{t_1}^{t_2} v_r dt \quad (4)$$

determined from consecutive pulsation cycles for long period Cepheids; short-period (likely overtone) Cepheids exhibit modulation on longer time-scales. Specifically,  $\ell$  Carinae exhibited a systematic difference of 5 – 6% between consecutive pulsation cycles. We stress that this effect is notably different from the *phase*-dependent  $p$ -factors discussed by Sabbey et al. (1995). Anderson (2014) discussed RV curve modulation in terms of a systematic uncertainty for BW distances, since  $\Delta R/p$  linearly enters  $d$  in Eq. 1. It remained unclear, however, how  $\Delta \Theta$  relates to cycle-to-cycle changes in  $\Delta R/p$ .

To answer this question, we started a monitoring campaign involving contemporaneous long-baseline interferometric and spectroscopic observations that operated between 2014 December 20 and 2015 May 22.  $\ell$  Carinae was chosen as the target for this campaign, since it subtends the largest angular size of any known Cepheid on the sky and since previous observations by Kervella et al. (2004d) and Davis et al. (2009) indicated that the instrumental precision of modern optical/NIR interferometers may be sufficient to reveal cycle-to-cycle differences at the order or magnitude indicated by the RV modulations.

In this paper, we investigate whether cycle-to-cycle differences are present in both the *angular* motion of *optical* layers traced by interferometry, and the *line-of-sight* or linear motion of *gas* layers traced by RVs, cf. Eq. 3. We describe our new observations in Sect. 2. Using these new observations, we first determine angular diameters from squared visibility curves in Sect. 3.1. We then study the RV variability in Sect. 3.2 using RVs determined by cross-correlation. We discuss our findings and their implications in Sect. 4 and conclude in Sect. 5. We provide supporting materials in Appendix A available in the electronic version of the journal.

## 2 OBSERVATIONS

We have gathered an unprecedented data set comprising 360 high-precision RVs derived from optical spectra and 15 high-precision angular diameters from NIR long-baseline interferometry. In this section, we describe the observations and resulting data sets.

### 2.1 VLTI/PIONIER High-precision Long-baseline Near-IR Interferometry

We carried out interferometric observations with the four-beam combiner *PIONIER* (Le Bouquin et al. 2011) at the Very Large Telescope Interferometer (VLTI, cf. Mérand et al. 2014) during

three observing runs in 2015 January and February (ESO Program ID 094.D-0583). The observations were taken near three epochs of predicted extremal diameter comprising two maxima and one minimum. We refer to these as max1, min1, and max2 in the remainder of this paper.

Our observations were aimed at determining angular diameters at successive extrema to test whether consecutive extrema would be significantly different, and how the full amplitude of angular diameter variations would behave if closely monitored. The motivation to carry out this investigation was given by observed cycle-to-cycle differences in the RV variability of four Cepheids (Anderson 2014).

We carried out all observations using all four 1.8 m Auxiliary Telescopes (ATs) placed to achieve the longest available baselines (up to 140 m, referred to here in units of mega- $\lambda$ ), aiming for the highest spatial frequencies to enable maximal spatial resolution. This was crucial for achieving the precision required for this program, since the longest baselines are just about capable of resolving the first zero of the visibility curves of  $\ell$  Carinae near its maximal diameter.

All measurements were taken with the recently installed *RAPID* detector<sup>1</sup>, which is optimized for fainter targets. In the medium sensitivity setting, we employed typical read-out times of 0.5 ms, which enabled up to 100 science object observations per half-night. All observations were taken in the new GRISM dispersion mode, which supplies six spectral channels in the  $H$  band (1.53, 1.58, 1.63, 1.68, 1.73, and 1.78  $\mu\text{m}$ ) with a spectral resolving power  $R \sim 45$ . Our typical (nightly) visibility curves for  $\ell$  Carinae contain approximately 500 data points.

We applied this extreme strategy in order to achieve the highest possible sensitivity to even the most minute cycle-to-cycle differences in the angular diameters. We followed the well-established observing strategy of alternating between observations of the science target and calibrator stars. During the first observing run (run A), this sequence was Cal1, Sci, Cal2, Sci, Cal1, etc. During later observing runs, we added additional calibrator stars. The calibrators common to all observations are HD 81502 and HD 89805. We calibrate our science observations using only the calibrator stars in common to all three observing runs, namely HD 81502 and HD 89805, and employ two other calibrators, namely HD 74088 and HD 81011, as *standard stars*, see the online Appendix A. Standard star observations are crucial for demonstrating that the precision and instrumental stability achieved are sufficient for identifying apparent cycle-to-cycle differences as features of the pulsations.

Table 1 lists all calibrator stars observed during our program. These were selected using the SearchCal tool (Bonneau et al. 2006, 2011) and/or taken from the catalog by Mérand et al. (2005) based on proximity on the sky, similar magnitude, and (where possible) accurately known diameters. Calibrators HD 90853, HD 102461, HD 102964, and HD 110458 are not used in this work, as they were observed only sporadically and/or variable stars.

The data reduction and calibration was performed using the *PIONIER* pipeline *pndrs*, adapted for the new detector. We cleaned the nightly time series, rejecting data that were obviously affected by meteorological conditions or technical problems such as the failing delay line DL4 (night of 2015 January 12) or if fringe tracking was temporarily lost. We removed a total of 700 of 10238

HD	Sep [deg]	$m_H$ [mag]	SpTyp	$\Theta_{UD}$ [mas]	$\sigma(\Theta_{UD})$ [mas]	Run
74088 <sup>†</sup>	7.65	3.15	K4III	1.493 <sup>a</sup>	0.019	C
81101 <sup>†</sup>	2.81	2.67	G6III	1.394 <sup>b</sup>	0.099	B,C
<b>81502</b>	3.42	3.24	K1.5II-III	1.230 <sup>d</sup>	0.016	A,B,C
<b>89805</b>	4.61	2.87	K2II	1.449 <sup>a</sup>	0.019	A,B,C
90853 <sup>1</sup>	6.46	2.96	F2II	1.025 <sup>b</sup>	0.072	B
102461 <sup>2</sup>	16.2	1.66	K5III	2.93 <sup>c</sup>	0.034	B
102964 <sup>‡</sup>	26.7	1.69	K3III	2.51 <sup>c</sup>	0.039	B
110458 <sup>‡</sup>	30.1	2.38	K0III	1.65 <sup>c</sup>	0.018	B

**Table 1.** Stars of known angular diameter observed contemporaneously with  $\ell$  Carinae. The two stars listed in bold font, HD 81502 and HD 89805, were observed during each observing run and are used to calibrate the measurements of  $\ell$  Carinae and any standard stars identified by <sup>†</sup>. Calibrators HD 102964 and HD 110458 (marked with <sup>‡</sup>) were disregarded due to their small number of observations. Notes on individual stars: <sup>1</sup>:  $s$  Carinae (not to be confused with variable star  $S$  Carinae) is a possible low-amplitude variable star (Stoy 1959) of unknown type. <sup>2</sup>: V918 Centauri, a variable star of unknown type with (*Hipparcos*-band) amplitude 0.0216 mag and frequency  $f = 0.05517$  (Koen & Eyer 2002). Origin of literature diameters: <sup>a</sup> Mérand et al. (2005), <sup>b</sup> Lafrasse et al. (2010), <sup>c</sup> Bordé et al. (2002).

UV points<sup>2</sup>. Once we completed outlier rejection, we used the *PIONIER* pipeline to compute squared visibilities  $V^2$ , triple product amplitudes, and triple product closure phases. In this work, we focus mainly on the derived squared visibilities. We studied  $\ell$  Carinae’s closure phase data using the python tool CANDID<sup>3</sup> (Galenne et al. 2015) to search for a close companion or signs of asymmetry, cf. Sect. 4.1. We also inspected closure phase stability of the calibrators and standard stars to ensure that these objects did not show any signs of companions.

Figure 1 shows the calibrated squared visibilities against projected baseline for the measurements of this program. Each row represents one epoch near an extremal diameter (max1, min1, max2) and the UV-plane coverage is shown in the top right corner of each night. Fig. 1 demonstrates the exquisite data quality achieved and helps to identify nights of better and worse quality. Uninterrupted observations and densely-covered UV-planes identify the better nights. The most crucial nights for comparing maximal radii were the three nights from 2015-01-09 through 2015-01-11 (marked max1) and 2015-02-14 through 2015-02-16 (marked max2).

Figure 1 also shows that the baseline configurations used are sufficient to resolve the first zero of the squared visibility curve during epochs near maximal diameter. Near minimal diameter, however, the first zero is not fully resolved.

We were extremely lucky not to suffer any completely lost night over the entirety of our 15 night observing program, with a total of 5 hours lost due to weather. Nevertheless, our data are of course subject to ambient conditions and other circumstances such as technical issues. We also note the failure of delay line 4 during observations on the night of 12 January. Inspection of the  $V^2$  curve from that night and the resulting diameter indicates that this night’s measurements are offset (biased) with respect to the other nights. While we cannot trace the reason for this outlier, we note a peculiar bifurcation in the visibility curve (Fig. 1) and the systematically higher  $\chi^2$  values (compared to the other nights of

<sup>1</sup> <http://www.eso.org/public/usa/announcements/ann15042/>

<sup>2</sup> Each observation supplies six UV points

<sup>3</sup> <https://github.com/amerand/CANDID>

Night	BL	Sky	Seeing [arcsec]	$\tau_{\text{coh}}$ [ms]	$t_{1,W}$ [h]	Tech
9 Jan	A1-G1-K0-I1	TN	0.7 – 1	1 – 2		
10 Jan	A1-G1-K0-I1	TK	1 – 1.5	$\sim 1$		
11 Jan	A1-G1-K0-I1	CY-TN	0.8 – 1.5	2 – 1	3	
12 Jan	A1-G1-K0-I1	TN	0.7 – 1.5	$< 2$		DL4
13 Jan	A1-G1-K0-I1	TK	$> 1$	$\sim 1$	2	
26 Jan	A1-G1-K0-I1	CL-WI	0.5 – 0.8	4 – 8		
27 Jan	A1-G1-K0-I1	CL-PH	1.5 – 2.5	$\sim 1$		
28 Jan	A1-G1-K0-I1	CL	0.5 – 1.2	2 – 3		
29 Jan	A1-G1-K0-I1	TN-CL	1 – 1.5	$< 2$		
30 Jan	A1-G1-K0-I1	TK-CL	0.5 – 1.3	$\sim 2$		
12 Feb	A1-G1-K0-J3	PH	$\sim 1$	$\sim 2$		
14 Feb	A1-G1-K0-J3	PH	1.7 – 1	2 – 4		
15 Feb	A1-G1-K0-J3	PH	0.5 – 1	4.5 – 3		
16 Feb	A1-G1-K0-J3	PH	1.3 – 1	2 – 4		
18 Feb	A1-G1-K0-J3	HU CL	1 – 2	$< 1$		

**Table 2.** Observation log for our VLTI/*PIONIER* program. Column BL lists the baseline configuration of the ATs, see <http://www.eso.org/sci/facilities/paranal/telescopes/vlti/configuration/P94.html.html> for more details. The information given for sky quality, seeing, etc. is given in chronological order per night. Sky quality is abbreviated as follows: TN = thin clouds, TK = thick clouds, CL = clear, CY = cloudy, WI = strong winds, PH = photometric, HU = high humidity. Column Seeing gives the range of DIMM seeing measured over the course of our observations.  $\tau_{\text{coh}}$  is the coherence time-scale of the atmosphere,  $t_{1,W}$  lists the time lost due to weather in hours, and Column Tech indicates nights with technical difficulties. Additional details are available through the ESO archive at <http://archive.eso.org/asm/ambient-server>.

this run) returned by the diameter fitting procedures (cf. Sect. 3.1). This does not constitute a problem for the present work, however, since we investigate primarily the three nights closest to maximum, see below. Table 2 provides an observing log for each night.



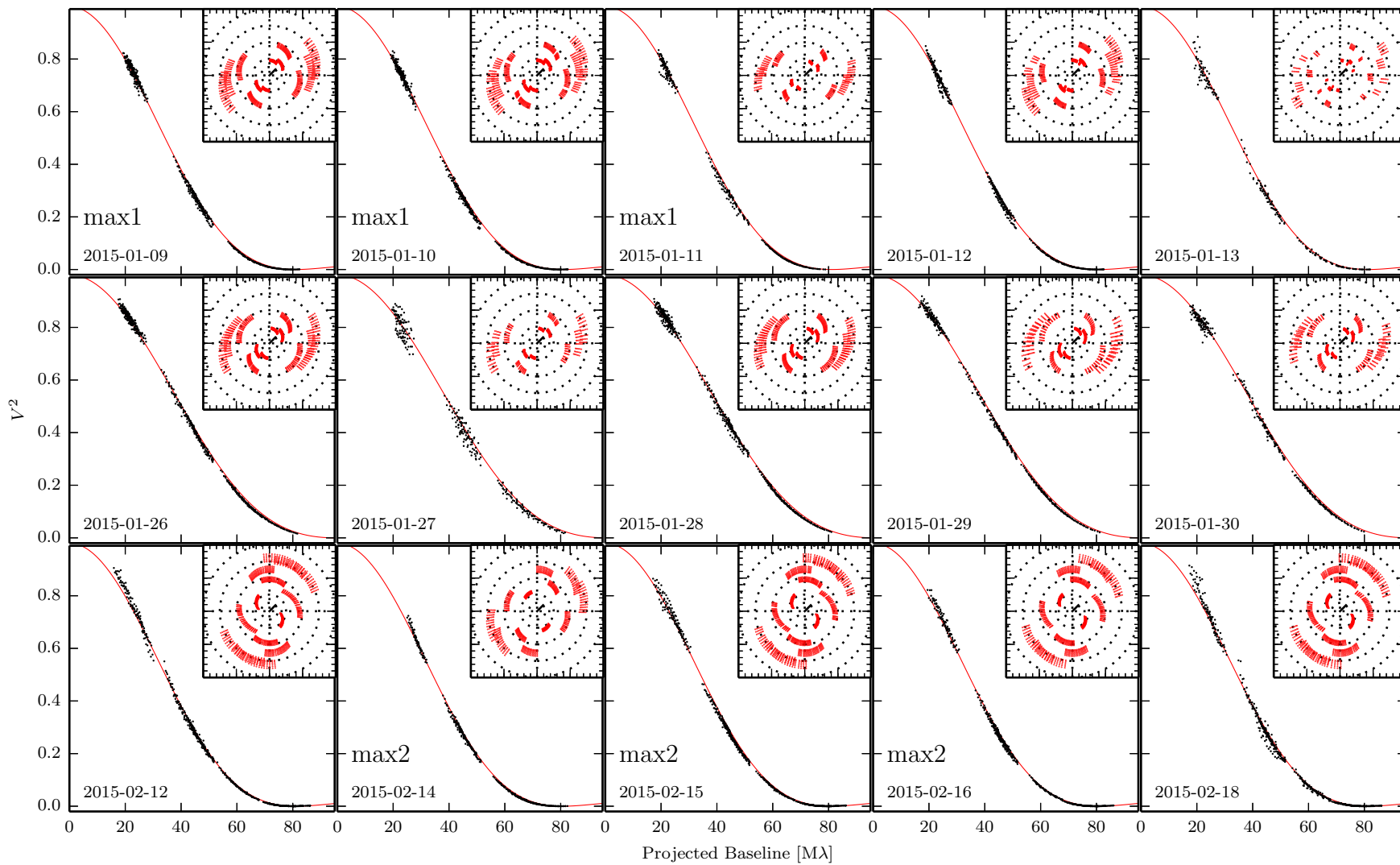


**Figure 1.** Squared visibilities against projected baselines in mega- $\lambda$  and UV plane coverage for all nights of program 094.D-0583. The axis range is 0 – 95  $M\lambda$  on the x-axis and –0.02 to unity on the y-axis. The local date of the beginning of each night is shown in the bottom left. The top panels show the epoch near the first maximum, followed by the epoch near minimal radius in the center panels, and the second maximum in the bottom row. The best-fitting uniform disk diameter fit is shown as a solid red curve. Nights near the first and second maximum are marked as max1 and max2, respectively. The UV-plane polar circles indicate 12.5, 25, 50, 75, and 100  $M\lambda$ .

BJD -2 400 000 d	$v_r$ [km s <sup>-1</sup> ]	$\sigma(v_r)$ [km s <sup>-1</sup> ]
57012.630987	19.603	0.005
57012.688859	19.623	0.004
57012.754012	19.636	0.004
57012.790623	19.630	0.004
57012.866436	19.628	0.004
57013.686595	19.259	0.004
57013.736319	19.221	0.004
57013.787895	19.174	0.004
57013.834101	19.106	0.003
57013.865421	19.069	0.004
...		
57158.496217	4.944	0.004
57158.641075	3.316	0.004
57159.494445	-4.971	0.004
57159.628088	-5.962	0.004
57160.493287	-10.866	0.004
57160.668815	-11.552	0.004
57162.489324	-15.003	0.004
57162.629240	-15.042	0.004
57164.525810	-14.314	0.004
57164.623180	-14.228	0.012

**Table 3.** Example data from our new (2014–2015) *Coralie* RV campaign. The first and last 10 measurements are shown. The full data set is made publicly available in the electronic version of the journal and through the CDS.

## 2.2 *Coralie* High-resolution Optical Spectra

We conducted optical high-resolution spectroscopic observations of  $\ell$  Carinae using the *Coralie* spectrograph (Queloz et al. 2001) at the Swiss 1.2 m Euler telescope located at La Silla Observatory, Chile. These observations served three primary purposes: (a) to quantify the line-of-sight component of  $\ell$  Carinae’s pulsations, i.e.,  $\Delta R/p$  (cf. Eq. 4), contemporaneously with the interferometric measurements; (b) to confirm the cycle-to-cycle modulations seen in 2014; (c) to provide precise timings for each cycle of contraction, expansion or full pulsation cycle (contraction and expansion). We typically aimed for three measurements per night, spaced out over the visibility of the object from La Silla Observatory to limit phase gaps introduced by the day/night cycle. Steeper and extremal parts of the RV curve were monitored more closely, with up to 10 observations in a given night. Our *Coralie* monitoring campaign began on 20 December 2014 and ended on 22 May 2015.

The raw data were reduced using the *Coralie* pipeline, which includes pre- and over-scan bias corrections, flat-fielding using halogen lamps, cosmic-clipping, and order extraction. The wavelength calibration is provided by thorium-argon lamp reference spectra. All observations were made in the OBTH observing mode, wherein a Th-Ar spectrum is interlaced between the orders of the science target via a secondary fiber to provide simultaneous corrections for RV zero-point drifts. This observing mode offers the highest precision. We determine RVs via the cross-correlation technique (Baranne et al. 1996; Pepe et al. 2003) using a numerical line mask representative of a solar spectral type. Table 3 shows a subset of our new RV measurements of  $\ell$  Carinae. The full data set is available in the electronic version of the journal as well as via the CDS.

*Coralie* received an upgrade in November 2014, before our monitoring began. During this upgrade, octagonal fibers were installed to replace the previously installed fibers with circular cross-sections, and a double-scrambler was reintroduced (F. Pepe 2014,

private communication). Octagonal fibers have been shown to yield higher precision RVs than circular ones (Bouchy et al. 2013), which is primarily attributed to better light scrambling as the light passes through the fiber into the spectrograph. The realignment of the optical path and the new optical fiber are expected to introduce a small zero-point offset with respect to *Coralie* RVs measured prior to the upgrade. Based on a monitoring of RV standard stars, this offset is on the order of 15 m s<sup>-1</sup>, but may depend on spectral type (F. Pepe private communication), and thus, may vary slightly as a function of pulsation phase. Since the upgrade was carried out before the RV monitoring campaign began, we expect no significant zero-point differences among the observations taken for this program. There may, however, exist small ( $\sim 15$  m s<sup>-1</sup>), possibly phase-dependent, differences between the *Coralie* RVs published by Anderson (2014) and the present ones.

RV uncertainties are determined by the *Coralie* pipeline and take into account photon noise as well as the shape of the CCF. In the case of the very bright ( $\langle m_V \rangle \sim 3.75$  mag, Fernie et al. 1995) star  $\ell$  Carinae, the derived uncertainty is limited by photon noise (Bouchy et al. 2001). The resulting typical uncertainties are on the order of a few m s<sup>-1</sup>, with median 3.14 m s<sup>-1</sup>. This is five times better than the measurements published in Anderson (2014), owing primarily to the different observing mode (OBTH).

We note that Cepheid atmospheres are much more complex than the atmospheres of stars to which this level of instrumental precision is usually applied, being subject to velocity gradients, turbulence, large scale convection, granulation, and possibly shock. In light of this, the above-stated uncertainties should not be mistaken for estimates of *accuracy* (cf. Lindegren & Dravins 2003), both because the measurement is biased and because no unique velocity applies to the entire atmosphere of the star.

In this work, we aim to determine differences in the behavior of pulsation cycles, i.e., we aim for the utmost *precision*. To this end, we adopt the definition that leads to the most *precise* estimate of (a weighted atmospheric average) RV. As shown by Anderson (2013) and reflected by the low scatter (during a single pulsation cycle) of the RV data presented here, so-called Gaussian RVs determined with the cross-correlation technique yield the most precise estimation of such mean velocities. We therefore adopt – as is also common practice – Gaussian RVs in this work. Further work (Anderson, in preparation) will provide additional insight into these questions.

## 3 RESULTS

We report the results of our observational program in this section, starting with the interferometric part in Sect. 3.1, followed by the results from spectroscopy in Sect. 3.2.

### 3.1 Modulated Interferometric Variability

The primary purpose of our observations for this paper is to obtain a differential measurement of  $\ell$  Carinae’s diameter determined near two consecutive maxima. To achieve the greatest possible precision, we obtained an unprecedented amount of observations with a state-of-the-art instrument, and aimed at avoiding observational biases as much as possible, e.g. by using the same calibrator stars for all observations.

We determined angular diameters  $\Theta$  by fitting squared visibility curves assuming both uniform disk ( $\Theta_{UD}$ ) and limb-darkened models. We determine  $\Theta_{UD}$  as well as diameters assuming linear

limb darkening  $\Theta_{\text{LD,lin}}$  using LITpro (Tallon-Bosc et al. 2008), a tool made freely available by the JMMC<sup>4</sup>. We adopt the fixed coefficient in the  $H$  band  $u_{\text{LD,H}} = 0.29$  for models assuming linear limb darkening (Neilson & Lester 2013).

We also determine limb darkened (Rosseland) diameters,  $\Theta_{\text{SATLAS}}$ , based on spherical SATLAS models (Neilson & Lester 2013), adopting a temperature range of 4700–5300 K for the phases covered by our observations (Luck et al. 2011). To this end, we compute  $V^2$  profiles using a numerical Hankel transform, taking into account bandwidth smearing effects. These limb-darkened diameters are likely the most *accurate* ever determined for a Cepheid variable star, given the amount of high-quality data used, mainly limited by assumptions on limb darkening and the wavelength solution. While we do adopt *phase-dependent* limb darkening laws (by adopting a range of  $T_{\text{eff}}$ ), we do not assume a *cycle-dependent* limb darkening law, since cycle-to-cycle differences in temperature at fixed pulsation phase are at least an order of magnitude smaller and will not significantly impact the result.

Table 4 lists the time series of the diameters we determined, as well as two measurements taken in between our program’s runs, when  $\ell$  Carinae was observed as a backup target<sup>5</sup>. The uncertainties listed in Tab. 4 are formal statistical uncertainties, i.e., do not take into account systematics such as the uncertainty of the wavelength calibration.

Since observations taken during the three nights closest to the maximal diameter do not vary significantly, we average these to determine more precise mean maximal diameters ( $\langle\Theta_{\text{max1}}\rangle$  and  $\langle\Theta_{\text{max2}}\rangle$ , cf. Tab. 5. We determine the standard mean error from the dispersion around that value, divided by  $\sqrt{3}$ . Figure 2 shows the angular diameters from Tab. 4 versus time relative to the closest time of maximal *linear* radius as determined from the RV curve, see Sect. 3.2.1. The enlarged inlays show the clearly offset, larger diameters of the second epoch near maximal diameter.

We thus determine a larger mean maximal diameter for the second epoch, differing by approximately  $22.5 \pm 1.4(\text{stat.})\mu\text{as}$ , or 0.7% of the second epoch’s diameter. We note that the cycle-to-cycle difference in maximal diameter is also apparent for UD diameters and diameters determined using a linear limb darkening law. While this difference is much larger than the squared sum of the scatter, we caution that other effects such as ablation due to rotation, small companions, or lack of instrumental stability could in principle introduce effects of this order. While we carried out several investigations into the robustness of this result, we unfortunately cannot *demonstrate* the long-term stability due to a lack of standard star observations during run A. We therefore conservatively consider this result *tentative* evidence for modulated angular variability.

At the extreme level of precision aimed for in this work, all possible sources of bias and instrumental effects must be taken into account (e.g. Kervella et al. 2004e). These include non-linear and time-dependent effects that can introduce unknown, albeit possibly significant, bias. Both types of systematics can in principle be traced by observations of standard stars. Time-dependent effects include shorter (intra-run) and longer (inter-run) effects. We performed the following tests to investigate whether the cycle-to-cycle differences are likely to be real. None of these tests indicated a spurious detection, i.e., they are all consistent with our result being a

true detection of cycle-to-cycle differences in the angular variability (see the online Appendix A for details). Specifically, we tested for:

- (i) the impact of the slightly different quadruplet baselines used at the two epochs near maximal diameter, since one station differed between run A (I1) and run C (J3), cf. Tab. 2;
- (ii) the impact of an asymmetric circumstellar envelope (CSE; Kervella et al. 2009). To this end, we discarded short baselines ( $V^2 > 0.5$ ) and re-determined diameters;
- (iii) the impact of the wavelength calibration. We investigate the intra-run stability for run C using HD 74088 and the intra-run stability (run B to C) using HD 81101. Since no standard stars were observed during run A, we unfortunately cannot demonstrate the stability of the inferred diameters over the full pulsation cycle. However, UD diameters of HD 81101 exhibit no systematic difference between run B and C;
- (iv) the impact of the fitting routine applied. We determine  $\Theta_{\text{UD}}$  and  $\Theta_{\text{LD,lin}}$  using LITpro and  $\Theta_{\text{SATLAS}}$  using an independent python routine as well as CANDID’s (Gallenne et al. 2015) functionality to determine diameters. While the face values of diameters determined with a given software may differ numerically, the clear cycle-to-cycle difference remains;
- (v) We test for companions of  $\ell$  Carinae (cf. Sect. 4.1) as well as calibrator/standard stars by inspecting closure phases;

Other possible sources of systematic effects are listed in Appendix A. Future observing runs will include additional standard star observations to monitor the stability of inferred diameters.

A real cycle-to-cycle difference between the two consecutive maximal diameters of  $\ell$  Carinae should lead to differences in brightness and color at the corresponding pulsation phase, since luminosity, radius, and temperature are linked to each other via the Stefan–Boltzmann law. We estimate the effect on both brightness and color while adopting a fixed value for the other. For an unchanged temperature, luminosity will vary by  $\sim 5\%$ , leading to a difference of approximately 10 mmag in the bolometric magnitude. For constant luminosity, the change in radius would lead to a decrease of 10 – 15 K in effective temperature, which will be challenging to detect spectroscopically. However, such a difference is likely detectable photometrically with the BRITe nanosatellites<sup>6</sup>, since it corresponds to a color difference of approximately  $\Delta(B - V) \approx 5$  mmag. Magnitude fluctuations on this order of magnitude have previously been reported using photometry from the MOST satellite (Evans et al. 2015) and, at a lower level, for V1154 Cygni with *Kepler* (Derekas et al. 2012), while Poretti et al. (2015) report only tentative detections of modulation based on *CoRoT* photometry of seven Cepheids. This illustrates the difficulty of detecting cycle-to-cycle differences, even with high-quality instruments due to the need for high instrumental stability over the time-scales of at least two pulsation cycles (more than two months for  $\ell$  Carinae).

## 3.2 Modulated Spectroscopic Variability

### 3.2.1 Radial Velocities

$\ell$  Carinae was among the targets for which Anderson (2014) discovered the modulated nature of Cepheid RV curves. Our new (2015)

<sup>4</sup> [http://www.jmmc.fr/litpro\\_page.htm](http://www.jmmc.fr/litpro_page.htm)

<sup>5</sup> We thank F. Antonioz for observing  $\ell$  Carinae as a backup target during ESO programme ID 094.C-0884(A).

<sup>6</sup> <http://brite-constellation.at/>

MJD	$\Theta_{\text{UD}}$ [mas]	$\sigma(\Theta_{\text{UD}})$ [mas]	$\chi^2_{\text{r,UD}}$	$\Theta_{\text{LDlin}}$ [mas]	$\sigma(\Theta_{\text{LDlin}})$ [mas]	$\chi^2_{\text{r,LDlin}}$	$\Theta_{\text{SATLAS}}$ [mas]	$\sigma(\Theta_{\text{SATLAS}})$ [mas]	$\chi^2_{\text{r,SATLAS}}$
57032.304901	3.09757	0.00029	2.13	3.1878	0.00037	3.10	3.2484 <sup>†</sup>	0.0004	4.153
57033.295435	3.09717	0.00026	1.48	3.1873	0.00032	2.12	3.2480 <sup>†</sup>	0.0004	2.930
57034.347907	3.09695	0.00031	1.49	3.1872	0.00036	1.85	3.2482 <sup>†</sup>	0.0004	2.606
57035.282871	<i>3.10028</i>	<i>0.00036</i>	2.89	<i>3.1948</i>	<i>0.00044</i>	3.89	3.2588 <sup>†</sup>	<i>0.0005</i>	5.589
57036.252418	3.08485	0.00052	1.33	3.1751	0.00060	1.62	3.2359 <sup>†</sup>	0.0007	2.089
57049.298269	2.63828	0.00028	0.82	2.7076	0.00030	0.91	2.7313 <sup>‡</sup>	0.0003	0.963
57050.260437	2.60085	0.00092	2.03	2.6687	0.00095	2.02	2.6918 <sup>‡</sup>	0.001	2.019
57051.304289	2.59989	0.00036	1.29	2.6675	0.00039	1.43	2.6905 <sup>‡</sup>	0.0004	1.498
57052.301669	2.60375	0.00026	0.76	2.6716	0.00027	0.81	2.6947 <sup>‡</sup>	0.0003	0.844
57053.308108	2.61558	0.00038	1.10	2.6829	0.00040	1.15	2.7058 <sup>‡</sup>	0.0004	1.183
57058.348365	2.84296	0.00247	0.91	2.9106	0.00255	0.92	2.9390*	0.0026	0.923
57059.356773	2.89133	0.00353	1.14	2.9599	0.00363	1.14	2.9887*	0.0037	1.137
57066.101811	3.09287	0.00021	2.66	3.1883	0.00026	3.74	3.2531 <sup>†</sup>	0.0003	5.128
57068.216931	3.11169	0.00030	3.10	3.2044	0.00034	3.76	3.2672 <sup>†</sup>	0.0004	4.854
57069.127975	3.10887	0.00019	3.01	3.2064	0.00025	4.35	3.2726 <sup>†</sup>	0.0003	6.186
57070.147921	3.11036	0.00027	3.62	3.2067	0.00034	4.85	3.2723 <sup>†</sup>	0.0004	6.55
57072.109906	3.08883	0.00031	1.54	3.1813	0.00041	2.44	3.2438 <sup>†</sup>	0.0005	3.418

**Table 4.** Angular diameters determined from our *PIONIER* observations. MJD is modified Julian date, i.e., JD  $-2\,400\,000.5$ . Subscripts UD and LD indicate uniform disk and limb darkened disk models, uncertainties given are the (underestimated, see the text in Sect. 3.1) statistical uncertainties, and all  $\chi^2$  values have been divided by the number of degrees of freedom. The measurements are grouped according to the epochs (max1, min1, in between, max2). Values shown in italics should be considered unreliable due to a technical problem with delay line 4. We adopt the following  $T_{\text{eff}}$  for the SATLAS models (Neilson & Lester 2013): <sup>†</sup>: 4700 K, \*: 5100 K, and <sup>‡</sup>: 5300 K (Luck et al. 2011).

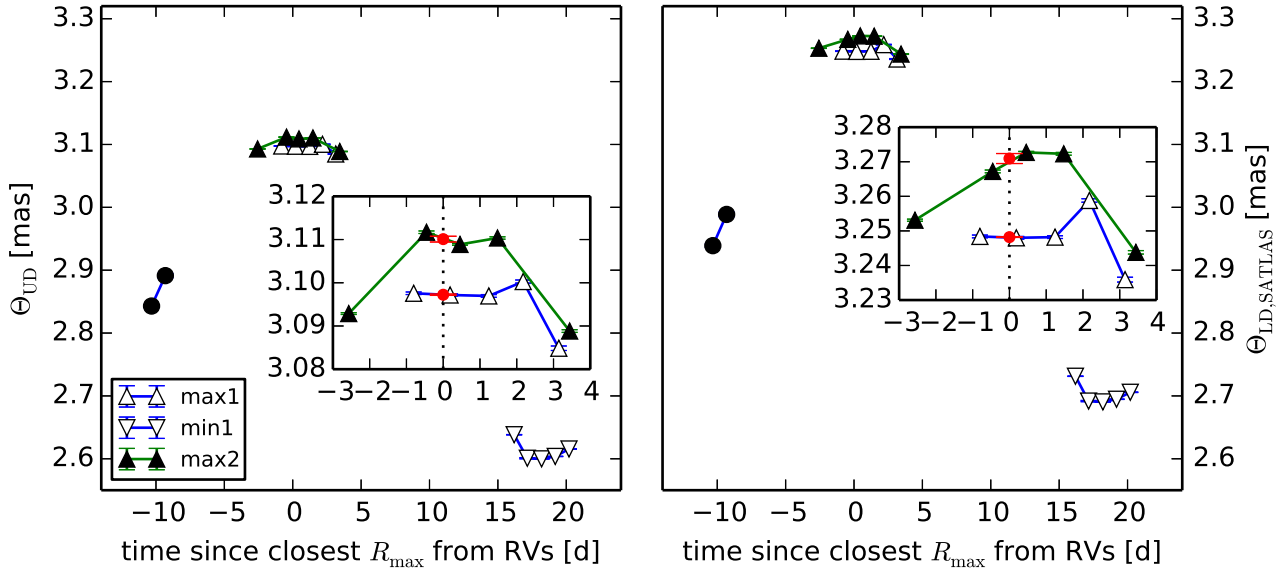
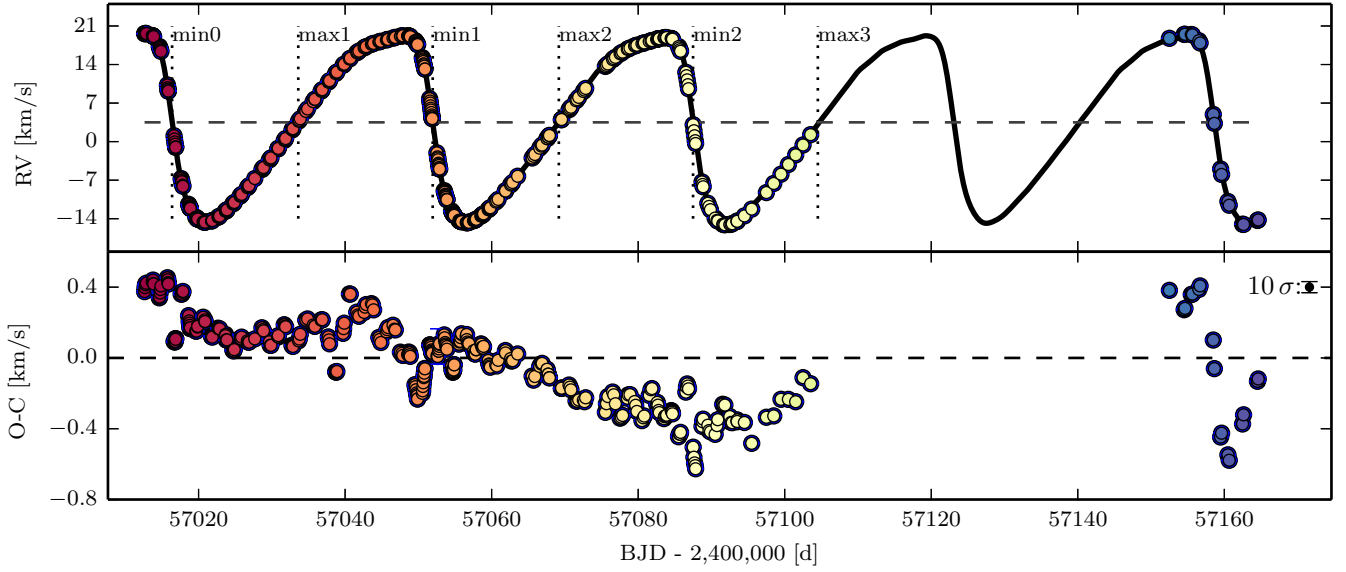


**Figure 2.** Tentative evidence for modulated nature of  $\ell$  Carinae’s variable angular diameters. We show diameters against time since the closest maximal *linear* radius as measured from the RV curve. Measurements near minimal, average, and maximal diameters are plotted as downward triangles, circles, and upward triangles, respectively. Open symbols denote earlier measurements. We show uniform disk diameters  $\Theta_{\text{UD}}$  in the left-hand panel and limb-darkened diameters (based on SATLAS models, cf. Tab. 4) in the right-hand panel. The measurements near maximum diameter suggest a systematic difference between the two consecutive observed maxima. The inlays in the center right of each panel are close-ups near maximum  $\Theta$ . The mean of the three measurements near each maximum is overplotted at time 0 as a red filled circle with the standard mean uncertainty determined from the dispersion of the points. The upward-offset open triangle near time 2 should be given low weight due to technical problems during that night, cf. Tabs. 2 and 4.

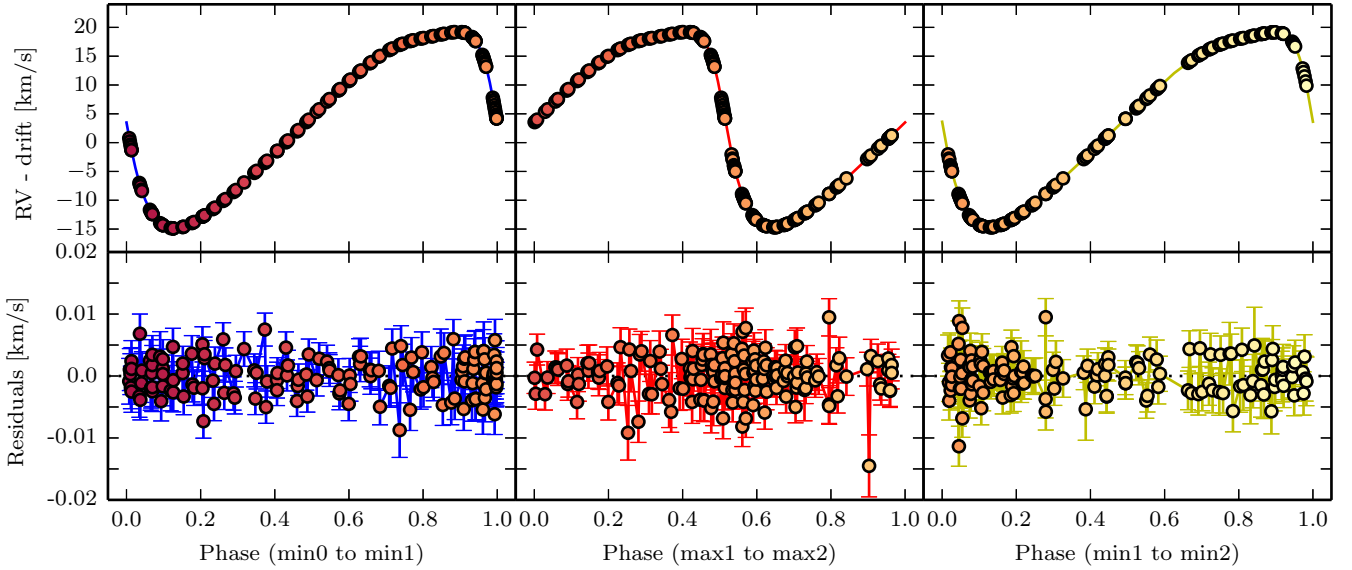
*Coralie* data presented here are approximately five times more precise than the 2014 data, owing mainly to contemporaneous RV drift corrections and to a lesser extent to an instrumental upgrade, cf. Sect. 2.2. As a result, our new data are particularly sensitive to RV curve modulation.

Figure 3 shows the new *Coralie* RV data obtained for

$\ell$  Carinae. The top panel shows the RV with respect to the Solar system barycenter against observation date and illustrates the unprecedented time sampling achieved over a period of 3 full months. We label epochs of extremal radii (min0, max1, min1, max2, max3), which we use for timing purposes in this work. We compute residuals as RV minus a best-fitting 12-th order Fourier series (fit-



**Figure 3.** The 2015 RV curve recorded for  $\ell$  Carinae against observation date. The top shows the barycentric RVs determined via the cross-correlation technique, with a color coding that traces the observation date (same in other related figures). Times near extremal diameters are indicated by min0, max1, min1, max2, min2, to inform the discussion in the text. A 12th-order Fourier series fit is shown as a black solid line, assuming pulsation period  $P = 35.5578$  d. The 10-fold median uncertainty is shown in the top right of the bottom panel. The bottom panel shows the residuals (data minus Fourier series fit), indicating a linear decrease in average RV during the continuously sampled part of the RV curve. This trend is not reproduced by the later, separate epoch observed near BJD 2457160.



**Figure 4.** The 2015 RV curve of  $\ell$  Carinae split into three separate parts, from min0 to min1 (left-hand panels), from max1 to max2 (center panels), and from min1 to min2 (right-hand panels). The linear drift shown in Fig. 3 was removed to determine times when the RV curve intersects the average velocity. Top panels show the RV data minus the drift as function of phase (within a given cycle). Bottom panels show the residuals of these data minus a cubic spline fit (shown as solid line in upper panels). The rms of the three residual panels is  $3.0 \text{ m s}^{-1}$ ,  $3.3 \text{ m s}^{-1}$ , and  $3.0 \text{ m s}^{-1}$  (the median RV uncertainty is  $3.14 \text{ m s}^{-1}$ ), respectively.

ted following [Anderson et al. 2013](#)). These residuals exhibit a linear trend over the duration of the continuous monitoring campaign. It is common to interpret such a linear variation in average RV as evidence for spectroscopic binarity (e.g. [Anderson et al. 2015](#)). We therefore obtained additional measurements in May 2015 to test whether the trend would continue. As the residuals demonstrate,

the additional (May) data are not consistent with a spectroscopic companion and show that the linear trend had stopped. We note that changes in pulsation period cannot explain this behavior. The recorded spectra exhibit cycle-to-cycle differences in the line profile variations that appear to be the leading origin of RV curve modulation, consistent with the interpretation that the apparent linear



Epoch	$\langle\Theta_{UD}\rangle$ [mas]	$\sigma(\langle\Theta_{UD}\rangle)$ [mas]	$\langle\Theta_{SATLAS}\rangle$ [mas]	$\sigma(\langle\Theta_{SATLAS}\rangle)$ [mas]
max1	3.0972	0.0001	3.2482	0.0001
max2	3.1103	0.0007	3.2707	0.0014
$\Delta_{\max}\Theta$	0.0131	0.0007	0.0225	0.0014

**Table 5.** Mean UD and limb-darkened diameters (based on SATLAS models, cf. Tab. 4) determined from the three nights closest to the maximal epoch together with their respective standard mean errors. The bottom row lists the difference in maximal diameter (max2 – max1) and the square-summed standard mean errors. The standard mean uncertainties do not reflect possible additional systematic uncertainty, see text. The difference in maximal limb-darkened diameters translates to a cycle-to-cycle difference of  $1.2 R_{\odot}$ .

Extremum	BJD - 2 400 000 [d]
min0	57016.386006
max1	57033.608096
min1	57051.957192
max2	57069.171281
min2	57087.491377
max3 <sup>†</sup>	57104.522379

**Table 6.** Epochs of extremal radius determined from the (trend-corrected) RV curve. <sup>†</sup> indicates that the epoch for max3 was determined by linear extrapolation over less than 1 d.

trend is not due to an unseen companion. An in-depth discussion of this effect will be presented separately (Anderson, in prep.).

To precisely determine epochs near extremal radii, knowledge of the intersection points of the RV curve and its average is required. Since the average velocity, usually referred to as  $v_{\gamma}$ , is *apparently* changing over the duration of our contemporaneous interferometric and spectroscopic observing campaign, we deem it appropriate to account for a time-variable  $v_{\gamma}$  when determining times of extremal radii. To this end, we represent the RV data before epoch max3 by a 12-th order Fourier series and a linear trend (slope  $m_{\text{drift}} = -8.0 \text{ m s}^{-1} \text{ d}^{-1}$ ). We subtract this trend from the RV data and from thereon treat the time series as having a constant  $v_{\gamma} = 3.500 \text{ km s}^{-1}$ .

We determine epochs of extremal radius from a cubic B-spline representation of the RV curve sampled at intervals of  $10^{-6} \text{ d}$  (0.086 s), which corresponds to the timing precision with which the spectra are recorded. Table 6 lists the timings of the extremal epochs thus determined. We note that subtracting the linear trend from the RV curve before determining epochs of extremal radius yields significantly smaller scatter in the cycle-to-cycle behavior of the pulsation period.

Figure 4 shows the RV curve of individual pulsation cycles between extrema min0 and max2, defined as running from either minimal radius to minimal radius or maximal to maximal radius over the duration of the VLTI campaign (ran from max1 to max2). The residuals in the lower panel have rms of approximately  $3 \text{ m s}^{-1}$  and show the excellent fit quality achieved by the spline model<sup>7</sup>.

<sup>7</sup> We chose spline models here, since Fourier series models exhibit ringing that overall yields a slightly less credible representation of the RV curve. While this effect is small, with a typical rms of  $6 \text{ m s}^{-1}$  when using Fourier series, we prefer the spline representation.

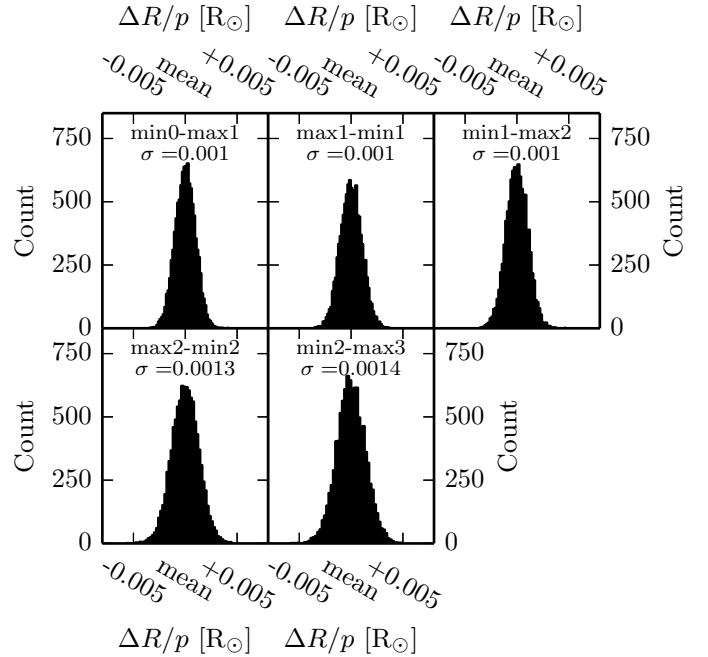


**Figure 5.** Distributions of  $\Delta R/p$  from 10000 Monte Carlo trials, centered on the respective means listed in Tab. 7. Standard deviations are indicated inside each panel.

We list the most relevant information regarding RV curve modulation in Table 7. We provide durations of consecutive expansion/contraction cycles, their RV amplitudes<sup>8</sup>, as well as the integral of the RV curve, i.e.,  $\Delta R/p$  (Eq. 4), determined using the timings from Tab. 6. We determine  $\Delta t$  and  $\Delta R/p$  as well as their uncertainties by means of a Monte Carlo experiment with 10000 trials. We show the distributions for  $\Delta R/p$  thus determined in Fig. 5, centered on the mean of the distribution. We determine RV amplitudes from the spline fit and list as a conservative uncertainty estimate the rms of the residuals rounded up to the next  $5 \text{ m s}^{-1}$ .

The values of  $\Delta t$  in Tab. 7 indicate that  $\ell$  Carinae contracts during  $\sim 51.5\%$  of its pulsation cycle. The durations also exhibit clear cycle-to-cycle variations. Such ‘jitter’ in pulsation periods has also been identified using space-based photometry of certain short period Cepheids, see Derekas et al. (2012) and Evans et al. (2015). We caution that the duration of the last expansion cycle (min2 to max3) appears to be significantly affected by the upturning RV residuals in Fig. 3, where the linear drift adds bias.

In addition to period jitter, Tab. 7 also clearly shows varying pulsation amplitudes, albeit at a much lower level than the one shown in Anderson (2014,  $\Delta A_{vr} = 0.51 \text{ km s}^{-1}$  between two consecutive cycles). We illustrate this by plotting two well-sampled sets of two consecutive pulsation cycles from 2014 and 2015 in Fig. 6, demonstrating the irregular and unpredictable nature of RV curve modulation. We point out that RV zero-point offsets (of order  $0.015 \text{ km s}^{-1}$ ) due to the instrumental upgrade are not responsible for this difference in amplitude. While all values of  $\Delta R/p$  deter-

<sup>8</sup> We refer to expansion and contraction cycles separately, since these enter BW distances via  $\Delta R$  and  $\Delta \Theta$ . The amplitudes of expansion and contraction cycles have to be added to obtain the total peak-to-peak amplitude of a full pulsation cycle.

From	Mean JD-2.4M [d]	$\Delta t$ [d]	$\sigma(\Delta t)$ [d]	$N_{\text{meas}}$	$A_{\text{RV}}$ [km s $^{-1}$ ]	$\sigma(A_{\text{RV}})$ [km s $^{-1}$ ]	$\Delta R/p$ [ $R_{\odot}$ ]	$\sigma(\Delta R/p)$ [ $R_{\odot}$ ]
min0 to max1	57023.222701	17.2211	0.0014	66	18.391	0.005	-24.0306	0.0095
max1 to min1	57045.413951	18.3521	0.0014	81	15.704	0.005	23.9752	0.0010
min1 to max2	57058.037466	17.2118	0.0013	85	18.181	0.005	-23.7519	0.0010
max2 to min2	57079.597885	18.3197	0.0013	57	15.651	0.005	23.6587	0.0013
min2 to max3 <sup>†</sup>	57092.907763	17.07	0.015	32	18.297	0.010	-23.7910	0.0020

**Table 7.** RV (semi-)amplitudes  $A_{\text{RV}}$  and RV curve integrals  $\Delta R/p$  determined from new *Coralie* data. The mean Julian date is that of the observations between consecutive extrema. The duration between extrema  $\Delta t$  and  $\Delta R/p$  as well as their uncertainties are determined from a Monte Carlo analysis with 10000 repetitions. RV (semi-)amplitudes  $A_{\text{RV}}$  are estimated from a spline fit (cf. Fig. 3 with a fixed adopted uncertainty of 5 m s $^{-1}$ , for an rms of approximately 3 m s $^{-1}$ . We used  $R_{\odot} = 696\,342 \pm 65$  km (Emilio et al. 2012). The <sup>†</sup> indicates that a linear extrapolation was used to determine the values for the last epoch (min2-max3), see Sect. 3.2.

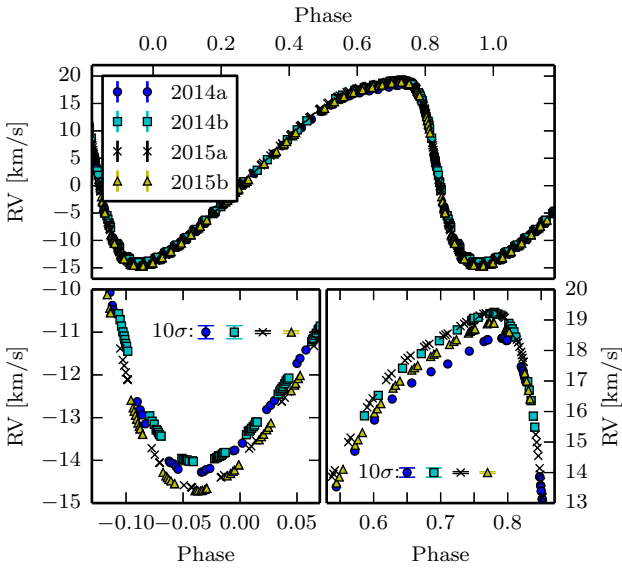


**Figure 6.** Comparison between 2014 and 2015 behavior of RV curve modulation. Data from two consecutive pulsation cycles from 2014 and 2015. 2014 data are shown as blue circles and cyan squares, data from 2015 as blue crosses (min0-min1) and yellow dots (min1-min2). In 2014, overall RV curve amplitudes were lower, but cycle-to-cycle differences were greater than in 2015. 10-fold median uncertainties shown in bottom panels.

mined from 2015 data are consistently larger than the ones from the year before, we note that the cycle-to-cycle variations were weaker in 2015.

Summing up the values for  $\Delta R/p$  determined in 2015, we find that RVs indicate an overall *decrease* in stellar radius of  $0.223 \pm 0.001 R_{\odot}$  between the epochs with contemporaneous interferometric measurements (max1 and max2), cf. Sect. 3.1, in contrast with the interferometric results. Taken at face value, the modulated RV curve indicates<sup>9</sup> a *decrease* of  $4.2 \mu\text{as}$  between epochs max1 and max2, i.e., an effect of different sign and amplitude compared to the angular diameter variability investigated above. One way to reconcile such a difference is by introducing a dependence of projection factors on pulsation cycles, cf. Sect. 4.2.

<sup>9</sup> assuming a “true”  $d = 497.5$  pc (value from Benedict et al. 2007) and  $p = 1.22$  from Breitfelder et al. (in preparation)

## 4 DISCUSSION

We now discuss these findings. First, we investigate whether the diameters we determine for  $\ell$  Carinae may be biased due to an unseen companion, finding no indication of this. Then, we discuss the implications of modulated angular and linear variability on BW distances.

### 4.1 Possible companion stars to $\ell$ Carinae

Based on the interferometric observations, we determine a detection limit of 0.15%, i.e.,  $\Delta m_H \approx 7$  mag, for any companions within  $\sim 50$  mas of  $\ell$  Carinae using the CANDID tool (Gallenne et al. 2015). At a distance of  $\sim 500$  pc this excludes bright companions with relative semimajor axis  $a_{\text{rel}} \lesssim 25$  AU.

Based on this detection limit and Geneva stellar evolution models (Ekström et al. 2012; Georgy et al. 2013; Anderson et al. 2014) of solar metallicity and average rotation, we estimate that  $\ell$  Carinae does not have a companion with mass greater than  $5 M_{\odot}$  (assuming  $9 M_{\odot}$  for  $\ell$  Carinae). The models predict  $M_H \approx -7.6$  mag for such a Cepheid on the third crossing of the instability strip, which is consistent with observations of rates of period change (Breitfelder et al. in prep.) and the absolute magnitude measured by Benedict et al. (2007). This provides an age estimate of approximately 35 Myr, which we use to inform the upper mass limit for a main sequence (MS) companion.

Possible companions with contrast ratios higher than 0.05% could in principle bias our result, while being undetectable in the interferometric data. This contrast ratio corresponds to a  $\sim 3.5 M_{\odot}$  MS star. Adopting an orbit with  $a_{\text{rel}} = 25$  AU (the detection window for CANDID), and a circular orbit, we find that such a hypothetical companion would have a semi-amplitude of  $> 1$  km s $^{-1}$  for inclination  $i > 10$  deg (e.g. 2 km s $^{-1}$  at  $i \sim 20$  deg) and orbital period of  $\sim 35$  yr. However, such a companion would be unlikely to bias the diameter estimate. Closer-in orbits would be more easily detectable due to higher RV semi-amplitude and shorter orbital periods. For instance, a semimajor axis of 3.5 AU ( $\sim 5$  times the radius of  $\ell$  Carinae) would have  $P_{\text{orb}} \sim 1.9$  yr, and orbital RV semi-amplitude in excess of 1 km s $^{-1}$  for almost all possible inclinations ( $i > 4$  deg.)

If one were to adopt the residual drift in RVs seen in Fig. 3 as a sign of spectroscopic binarity, then this would yield an estimate of the orbital period in the range of approximately 160 d. We estimate a minimum mass of approximately  $0.05 M_{\odot}$  for an edge-on orbit with this period and  $K_1 \sim 400$  m s $^{-1}$ . For a companion star of more significant mass, the orbit would have to be seen nearly face on for

combination	$\Theta_{\text{LD,max}}$ [mas]	$\Theta_{\text{LD,min}}$ [mas]	$\Delta\Theta$ [mas]	$\Delta R/p$ [ $R_{\odot}$ ]	$p$
max1 to min1	3.2482	2.6905	0.5577	23.9752	1.24
min1 to max2	3.2707	2.6905	0.5802	23.7519	1.31
max1 to max2			1.1379	47.7271	1.2741

**Table 8.**  $p$ -factors calculated separately for contraction and expansion, and for the full pulsation cycle (sum of the two) based on our fully contemporaneous data set. We here adopt  $d = 497.5$  pc as *true* distance to showcase the impact of modulated variability on  $p$ -factors. We use the limb-darkened diameters based on SATLAS models, cf. Tab. 4. The accuracy of  $p$ -factors is currently limited by errors on distance ( $\sim 10\%$ ).

this not to cause enormous RV variations. Within the range of the residuals, only inclinations  $< 1$  deg would be allowed. However, such an orbit would result in significant tidal forces that would significantly distort  $\ell$  Carinae, leading to hotter polar regions. Due to the (hypothetical) low inclination, one would thus expect  $\ell$  Carinae as an abnormally hot Cepheid. Contrastingly,  $\ell$  Carinae is among the coolest known Cepheids, i.e., this prediction is inconsistent with the available evidence.

It is thus highly unlikely that our diameter measurements of  $\ell$  Carinae are biased by an unseen companion. Low-mass companions on long-period orbits remain possible, however. *Gaia*’s ongoing observations of  $\ell$  Carinae will be useful for further exploring the parameter space of possible companions to  $\ell$  Carinae.

#### 4.2 Importance for Baade-Wesselink distances

As described above, we find tentative evidence for  $\ell$  Carinae’s different maximal angular diameters measured from two consecutive pulsation cycles. Contemporaneously, we have confirmed its modulated variability in RV. While interferometric measurements suggest (at face value) an *increase* in maximal diameter from the first to the second maximum (by approximately  $22.5 \mu\text{as}$  for limb darkened diameters), the modulated RV curve suggests a variation with opposite sign and smaller amplitude.

If confirmed by further interferometric measurements, this discrepancy could be explained by differences in the motion of *gas* layers (traced by RVs) and *optical* layers (interferometry traces motion of the continuum). Following Nardetto et al. (2007), this difference enters into the definition of the projection factor, which is used to translate measured line-of-sight velocities to pulsation velocities, cf. the factor  $f_{o-g}$  in Eq. 3. Our result would thus imply a time-dependence in the differential motion between the optical and gas motions, rendering  $f_{o-g}$  time-dependent, i.e., differing between one contraction or expansion cycle and the following expansion or contraction.

To quantify the possible difference in  $p$ -factor caused by differentially moving layers, we consider the following scenarios in which we determine  $p$  using (a “true” distance of)  $d = 497.5$  pc (Benedict et al. 2007, the uncertainty of approximately 10% is neglected for this thought experiment), and the three possible combinations of  $\Delta\Theta$  and  $\Delta R/p$  measured contemporaneously. We list the results in Tab. 8.

These examples illustrate how cycle-to-cycle variations in  $\Delta\Theta$  and the integrated RV curve lead to differences in  $p$  of up to 5%, even between successive contractions and expansions. This significant difference must be overcome to enable BW distances accurate to 1%, since BW distances depend linearly on  $p$ . However, cycle-to-cycle variations in  $\ell$  Carinae thus far appear to be stochastic

(based on the 2014 and 2015 RV data). It therefore seems likely that such effects largely cancel out when using data covering a larger temporal baseline. This is the approach used in analyses based on the SPIPS code (Mérand et al. in press; Breiterfeldt et al. in prep.).

If not somehow avoided or corrected for, the modulated variability of  $\ell$  Carinae and other Cepheids could lead to an increased scatter of PLRs calibrated using BW distances. Decreasing the scatter of PLRs is, however, crucial for separating luminosity differences due to line-of-sight and metallicity effects in Cepheids located in the Magellanic clouds.

## 5 CONCLUSIONS

We have carried out an unprecedented 3-month-long interferometric (VLTI/*PIONIER*) and spectroscopic (*Coralie*) monitoring campaign aimed at characterizing the modulated variability of the long-period Cepheid  $\ell$  Carinae.

The following summarizes our key results.

(i) We find the first tentative evidence of cycle-to-cycle differences in the *angular* diameter variability of a pulsating star. The two maximal (limb-darkened) angular diameters determined from two consecutive epochs spanning maximal diameters differ by  $22.4 \pm 1.4(\text{stat.}) \mu\text{as}$ . Our results suggest the second maximum to subtend a larger angle. While certain systematic effects could render this result spurious, none of the tests that we were able to carry out indicated such bias.

(ii) If real, this difference in maximal angular diameter can lead to photometric variations at this pulsation phase on the order of  $\sim 10$  mmag in bolometric magnitude, or 5 mmag in  $(B - V)$  color. Fluctuations on this order have been detected in short-period Cepheids by Derekas et al. (2012) and Evans et al. (2015).

(iii) We confirm the presence of RV curve modulation reported by Anderson (2014). Our new observations have approximately five times higher precision. We find a lower level of RV curve modulation than in 2014, although overall RV amplitudes are larger, indicating an irregular modulation. We find that RV curve modulation can under certain circumstances be misinterpreted as evidence for spectroscopic binarity.

(iv) Our results suggest that angular diameter and linear radius variations are modulated at different amplitudes and (in this case) with opposite sign. Such behavior is likely indicative of the different motion undergone by the *optical* continuum traced interferometrically and the *gas* traced via RVs. This different motion enters the definition of the projection factor as a factor  $f_{o-g}$ , see Nardetto et al. (2007) and Eq. 3. Our result thus suggests that  $f_{o-g}$  is time-dependent, varying by approximately 5% between successive expansion and contraction cycles. The irregular behavior of the RV curve modulation suggests a complex time-dependence of  $p$ -factors.

(v) We use interferometric measurements to set an upper limit of  $5 M_{\odot}$  for any potential companion stars.

Our detailed spectro-interferometric investigation reveals previously hidden complexities of Cepheid pulsations that open a new window for understanding the variability of classical Cepheids. Additional observations are required to investigate the long-term behavior of the modulated variability as well as any possible periodicity. To this end, high-quality interferometric, multi-band photometric, and high-precision velocimetric data are needed.

Greater angular resolution, enabled by larger interferometric baselines such as those offered by the *CHARA* array or high-

precision instruments such as the future *GRAVITY* instrument at ESO VLTI provide access to expanding this kind of study to additional Cepheids. High-quality photometry will soon be provided by the *BRITe* nano-satellites. Optical spectrographs capable of delivering  $\text{m s}^{-1}$  precision are becoming more common thanks to the developments driven by the search for extra-solar planets. Finally, *Gaia* and *Hubble Space Telescope* (Riess et al. 2014) will soon deliver Cepheid parallaxes of unprecedented accuracy. This fortuitous combination of instruments delivering unprecedented data quality will enable significant improvements for Baade-Wesselink distances in the near future, which will enable detailed investigations of the effect of chemical composition on the period-luminosity relation.

## ACKNOWLEDGMENTS

We thank the anonymous referee for her/his report. We acknowledge the Euler team at Geneva Observatory and La Silla Observatory for ensuring smooth operations and the Geneva exoplanet group for providing support. We thank (in chronological order) A.H.M.J. Triaud, S. Péretti, J. Cerda, D. Martin, V. Mégevand, L. Weber, J. Jenkins, and V. Bonvin for carrying out observations as part of the RV monitoring campaign. We also thank the director of Geneva Observatory, S. Udry for agreeing to such a dedicated, long-term effort. We greatly appreciated the friendly and competent assistance by ESO staff at ESO La Silla and Paranal Observatories.

RIA acknowledges funding from the Swiss National Science Foundation. PK, AM, JB, and AG acknowledge financial support from the “Programme National de Physique Stellaire” (PNPS) of CNRS/INSU, France. PK and AG acknowledge support of the French-Chilean exchange program ECOS-Sud/CONICYT. AG acknowledges support from FONDECYT grant 3130361. This research received the support of PHASE, the partnership between ONERA, Observatoire de Paris, CNRS and University Denis Diderot Paris 7. The Euler telescope is supported by the Swiss National Science Foundation.

This research has made use of the following services provided Jean-Marie Mariotti Center services *Aspro*<sup>10</sup> and *SearchCal*<sup>11</sup>, co-developed by FIZEAU and LAOG/IPAG, as well as of the CDS Astronomical Databases SIMBAD and VizieR catalogue access tool<sup>12</sup> and NASA’s Astrophysics Data System.

## REFERENCES

- Anderson R. I., 2013, PhD thesis, Université de Genève
- Anderson R. I., 2014, *A&A*, **566**, L10
- Anderson R. I., Eyer L., Mowlavi N., 2013, *MNRAS*, **434**, 2238
- Anderson R. I., Ekström S., Georgy C., Meynet G., Mowlavi N., Eyer L., 2014, *A&A*, **564**, A100
- Anderson R. I., Sahlmann J., Holl B., Eyer L., Palaversa L., Mowlavi N., Süveges M., Roelens M., 2015, *ApJ*, **804**, 144
- Baade W., 1926, *Astronomische Nachrichten*, **228**, 359
- Baranne A., et al., 1996, *A&AS*, **119**, 373
- Becker W., 1940, *ZAp*, **19**, 289
- Benedict G. F., et al., 2007, *AJ*, **133**, 1810
- Bonneau D., et al., 2006, *A&A*, **456**, 789
- Bonneau D., Delfosse X., Mourard D., Lafrasse S., Mella G., Cetre S., Clausse J.-M., Zins G., 2011, *A&A*, **535**, A53
- Bordé P., Coudé du Foresto V., Chagnon G., Perrin G., 2002, *A&A*, **393**, 183
- Bouchy F., Pepe F., Queloz D., 2001, *A&A*, **374**, 733
- Bouchy F., Díaz R. F., Hébrard G., Arnold L., Boisse I., Delfosse X., Peruchot S., Santerne A., 2013, *A&A*, **549**, A49
- Davis J., Jacob A. P., Robertson J. G., Ireland M. J., North J. R., Tango W. J., Tuthill P. G., 2009, *MNRAS*, **394**, 1620
- Derekas A., et al., 2012, *MNRAS*, **425**, 1312
- Ekström S., et al., 2012, *A&A*, **537**, A146
- Emilio M., Kuhn J. R., Bush R. I., Scholl I. F., 2012, *ApJ*, **750**, 135
- Evans N. R., et al., 2015, *MNRAS*, **446**, 4008
- Feast M. W., Catchpole R. M., 1997, *MNRAS*, **286**, L1
- Fernie J. D., Evans N. R., Beattie B., Seager S., 1995, *Information Bulletin on Variable Stars*, **4148**, 1
- Fouqué P., Gieren W. P., 1997, *A&A*, **320**, 799
- Freedman W. L., Madore B. F., Scowcroft V., Burns C., Monson A., Persson S. E., Seibert M., Rigby J., 2012, *ApJ*, **758**, 24
- Gallenne A., et al., 2015, *A&A*, **579**, A68
- Georgy C., Ekström S., Granada A., Meynet G., Mowlavi N., Eggenberger P., Maeder A., 2013, *A&A*, **553**, A24
- Groenewegen M. A. T., 2008, *A&A*, **488**, 25
- Groenewegen M. A. T., 2013, *A&A*, **550**, A70
- Hinshaw G., et al., 2013, *ApJS*, **208**, 19
- Hoffmann S. L., Macri L. M., 2015, *AJ*, **149**, 183
- Humphreys E. M. L., Reid M. J., Moran J. M., Greenhill L. J., Argon A. L., 2013, *ApJ*, **775**, 13
- Kervella P., Coudé du Foresto V., Perrin G., Schöller M., Traub W. A., Lacasse M. G., 2001, *A&A*, **367**, 876
- Kervella P., Nardetto N., Bersier D., Mourard D., Coudé du Foresto V., 2004a, *A&A*, **416**, 941
- Kervella P., Bersier D., Mourard D., Nardetto N., Coudé du Foresto V., 2004b, *A&A*, **423**, 327
- Kervella P., Bersier D., Mourard D., Nardetto N., Fouqué P., Coudé du Foresto V., 2004c, *A&A*, **428**, 587
- Kervella P., Fouqué P., Storm J., Gieren W. P., Bersier D., Mourard D., Nardetto N., du Coudé Foresto V., 2004d, *ApJ*, **604**, L113
- Kervella P., Coudé du Foresto V., Segransan D., di Folco E., 2004e, in Traub W. A., ed., *Society of Photo-Optical Instrumentation Engineers (SPIE) Conference Series* Vol. 5491, *New Frontiers in Stellar Interferometry*, p. 741
- Kervella P., Mérand A., Gallenne A., 2009, *A&A*, **498**, 425
- Koen C., Eyer L., 2002, *MNRAS*, **331**, 45
- Lafrasse S., Mella G., Bonneau D., Duvert G., Delfosse X., Chesneau O., Chelli A., 2010, in *Society of Photo-Optical Instrumentation Engineers (SPIE) Conference Series*, p. 4 ([arXiv:1009.0137](https://arxiv.org/abs/1009.0137)), doi:10.1117/12.857024
- Le Bouquin J.-B., et al., 2011, *A&A*, **535**, A67
- Leavitt H. S., 1908, *Annals of Harvard College Observatory*, **60**, 87
- Leavitt H. S., Pickering E. C., 1912, *Harvard College Observatory Circular*, **173**, 1
- Lindgren L., Dravins D., 2003, *A&A*, **401**, 1185
- Lindemann F. A., 1918, *MNRAS*, **78**, 639
- Luck R. E., Andrievsky S. M., Kovtyukh V. V., Gieren W., Graczyk D., 2011, *AJ*, **142**, 51
- Macri L. M., Stanek K. Z., Bersier D., Greenhill L. J., Reid M. J., 2006, *ApJ*, **652**, 1133
- Macri L. M., Ngeow C.-C., Kanbur S. M., Mahzooni S., Smitka M. T., 2015, *AJ*, **149**, 117
- Mérand A., Bordé P., Coudé du Foresto V., 2005, *A&A*, **433**, 1155
- Mérand A., et al., 2014, in *Society of Photo-Optical Instrumentation Engineers (SPIE) Conference Series*, p. 0 ([arXiv:1407.2785](https://arxiv.org/abs/1407.2785)), doi:10.1117/12.2057150
- Nardetto N., Fokin A., Mourard D., Mathias P., Kervella P., Bersier D., 2004, *A&A*, **428**, 131
- Nardetto N., Mourard D., Mathias P., Fokin A., Gillet D., 2007, *A&A*, **471**, 661

<sup>10</sup> Available at <http://www.jmmc.fr/aspro>

<sup>11</sup> Available at <http://www.jmmc.fr/searchcal>

<sup>12</sup> Available at <http://cdsweb.u-strasbg.fr/>



- Neilson H. R., Lester J. B., 2013, *A&A*, **554**, A98
- Nordgren T. E., Armstrong J. T., Germain M. E., Hindsley R. B., Hajian A. R., Sudol J. J., Hummel C. A., 2000, *ApJ*, **543**, 972
- Pepe F., Bouchy F., Queloz D., Mayor M., 2003, in Deming D., Seager S., eds, *Astronomical Society of the Pacific Conference Series Vol. 294*, Scientific Frontiers in Research on Extrasolar Planets. pp 39–42
- Planck Collaboration et al., 2014, *A&A*, **571**, A16
- Poretti E., Le Borgne J.-F., Rainer M., Baglin A., Benko J., Debosscher J., Weiss W. W., 2015, preprint, ([arXiv:1508.07639](https://arxiv.org/abs/1508.07639))
- Queloz D., et al., 2001, *The Messenger*, **105**, 1
- Riess A. G., et al., 2011, *ApJ*, **730**, 119
- Riess A. G., Casertano S., Anderson J., MacKenty J., Filippenko A. V., 2014, *ApJ*, **785**, 161
- Sabbe C. N., Sasselov D. D., Fieldus M. S., Lester J. B., Venn K. A., Butler R. P., 1995, *ApJ*, **446**, 250
- Scowcroft V., Freedman W. L., Madore B. F., Monson A., Persson S. E., Rich J., Seibert M., Rigby J. R., 2015, preprint, ([arXiv:1502.06995](https://arxiv.org/abs/1502.06995))
- Soszynski I., et al., 2008, *Acta Astron.*, **58**, 163
- Storm J., Carney B. W., Gieren W. P., Fouqué P., Latham D. W., Fry A. M., 2004, *A&A*, **415**, 531
- Storm J., et al., 2011, *A&A*, **534**, A94
- Stoy R. H., 1959, *Monthly Notes of the Astronomical Society of South Africa*, **18**, 48
- Suyu S. H., et al., 2012, preprint, ([arXiv:1202.4459](https://arxiv.org/abs/1202.4459))
- Tallon-Bosc I., et al., 2008, in *Society of Photo-Optical Instrumentation Engineers (SPIE) Conference Series*. p. 1, doi:10.1117/12.788871
- Wesselink A. J., 1946, *Bull. Astron. Inst. Netherlands*, **10**, 91
- van Leeuwen F., Feast M. W., Whitelock P. A., Laney C. D., 2007, *MNRAS*, **379**, 723

## APPENDIX A: SUPPORTING EVIDENCE FOR MODULATED ANGULAR VARIABILITY

This appendix provides details of the tests we carried out to investigate the precision of the diameters inferred from our interferometric measurements and the instrumental stability. This is a crucial step in determining whether the minute cycle-to-cycle differences between the maximal diameters subtended by  $\ell$  Carinae are real or explained by systematics. While the accuracy of angular diameter measurements is dominated by the accuracy of the wavelength calibration and the treatment of limb darkening, significantly higher *precision* may be achieved by eliminating sources of bias via a differential measurement. The tentative evidence for such cycle-to-cycle variations presented here relies on such a differential measurement involving the mean maximal diameters determined during the consecutive runs A and C.

The following elements involved in the observation affect the precision of this differential measurement. These can be separated into effects acting on intra-run time-scales ( $< 10$  d) and inter-run time-scales ( $> 10$  d). Intra-run effects include

- (i) nightly wavelength calibrations (can be traced via standard stars);
- (ii) choice of calibrator stars (avoided by using common set of calibrator stars);
- (iii) sampling of UV-plane, i.e., projected baselines;
- (iv) telescope or instrument vibrations (should mainly cancel out over half-nights of observations);
- (v) pupil stability (affects baseline stability).

Any biases introduced by such effects should affect all stars observed during a given night in the same way. Standard star observations, i.e., treating calibrator stars of known high stability as science targets, thus provide a means to monitor the stability and the

precision that can be achieved during a given observing run. If the same standard star was observed during multiple observing runs, this information can be used to track instrumental stability over a longer timeframe. We perform such a test in Appendix A1 below, finding excellent inter-run precision for standard star HD 74088 and no significant offsets between runs B and C for standard star HD 81101.

Inter-run effects (mainly introduced by observations at different azimuthal angles) include the following.

- (i) All intra-run effects listed above.
- (ii) Stellar companions to  $\ell$  Carinae although Sect. 4.1 excludes this possibility.
- (iii) Stellar companions to calibrator stars, in analogy with the effect stated above for the science target. Using more than one calibrator per run (as we did) reduces the impact of such an effect. We additionally inspect the closure phase measurements for all standard stars in Appendix A4 below.
- (iv) Stellar ablation due to rotation (calibrators and science target) can yield similar intra-run differences due to different viewing angles. However, rotation is expected to be very slow for all calibrator stars used (late-type giant stars) as well as for  $\ell$  Carinae. Nevertheless,  $\ell$  Carinae's  $v \sin i \approx 7 \text{ km s}^{-1}$  may lead to a flattening on the order of 0.2–0.3% (assuming a Roche model with  $8 M_{\odot}$  and  $180 R_{\odot}$ ), i.e., around  $7.5 \mu\text{as}$ .
- (v) Possible surface inhomogeneities (spots).
- (vi) Changes in the instrumental setup: mirror coatings (ageing effects, re-coatings of individual mirrors), optical defects, polarization.
- (vii) asymmetric circumstellar envelopes (CSE). CSEs mainly affect short baseline and the top part of the  $V^2$  curve. We therefore discarded short baselines and re-determined diameters with only long baselines, but found virtually no difference with the result based on all baselines, cf. Appendix A2.
- (viii) Different baseline configurations used. One AT was located at different stations during runs A (station I1) and C (station J3). We investigate whether this result might introduce a bias in Appendix A3, and find no sign of a bias.

Unfortunately, no standard star observations are available for run A, precluding a final assessment of any inter-run differences between run A and run C. While all of our tests indicate that there is no cause for alarm<sup>13</sup>, we acknowledge that there remains room for systematics that can lead to a spurious result, since we cannot *demonstrate* the absence of inter-run biases between run A and C. We thus conservatively consider the evidence for modulated angular diameter variability as tentative and call for prudence in the interpretation of this result. To improve this situation in the future, we plan to observe the standard stars HD 74088, HD 81011 during all future observing runs in order to identify and monitor instrumental effects and distinguish them clearly from real modulated variability.

### A1 Intra- and Inter-run Stability of Inferred Diameters determined using Standard stars

Using the calibrator star HD 74088 as a *standard*<sup>14</sup> star, we investigate the stability of UD diameters over the timespan of one run, specifically run C. Figure A1 shows the UD diameters determined

<sup>13</sup> This one is for VLT observers

<sup>14</sup> i.e., we treated it as a science object, calibrating the visibilities with the same stars that were used for  $\ell$  Carinae.



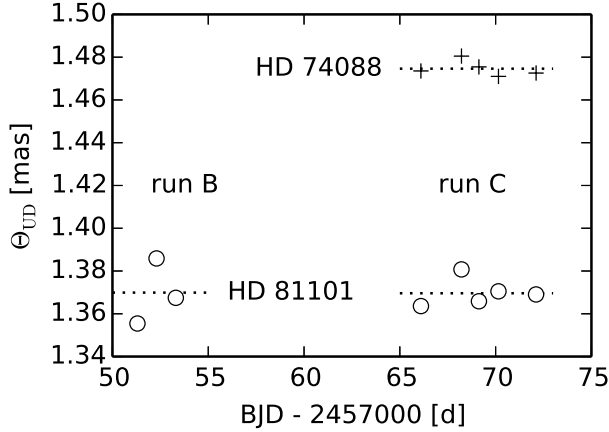


**Figure A1.** Time series of angular diameters for standard stars. HD 74088 is plotted as black pluses and indicates excellent intra-run stability ( $\sim 0.0015$  mas). HD 81101 is plotted as black open circles and can be used to trace inter-run stability. There is no significant difference between runs B and C for HD 81101 and HD 74088 and this demonstrates excellent intra-run stability.

with LITPro as black pluses. We find  $\langle \Theta \rangle = 1.4746 \pm 0.0015$  mas over the five nights. This indicates excellent intra-run stability and corroborates the use of mean diameters for investigating the modulated variability of  $\ell$  Carinae.

Analogously, we use HD 81101 (observed during runs B and C) to test the inter-run stability of UD diameters. Figure A1 shows these diameters as open circles. We find no significant difference between the diameters determined during runs B and C, with a difference of  $0.0004 \pm 0.0068$ . The absence of any inter-run differences corroborates the apparent cycle-to-cycle difference of the maximal diameters.

Unfortunately, we do not have a sufficient number of calibrator stars available to perform this test for runs A and C. We did, however, perform a test where we calibrated each calibrator with the other and checked for the stability of the result. Of course, the results of this test are not independent, since a bias in either calibrator will directly affect the ‘science’ target. Nevertheless, we find no clear signs of systematic differences between runs A and C; the offsets between both runs are each approximately  $8 \mu\text{as}$ , with opposite sign. We find standard mean errors during each run of  $3 - 5 \mu\text{as}$  for both stars. This example shows the importance of observing additional calibrator stars as standards to trace the instrumental stability.

## A2 Removing short baselines with $V^2 > 0.5$ for $\ell$ Carinae

Here we test the sensitivity to a possible circumstellar environment by discarding measurements at short baselines. We list the inferred UD diameters in Tab. A1 and show the  $V^2$  curves in Fig. A2. We obtain results that are virtually identical to the UD diameters in Tab. 4 and find a clear (formal) difference between the diameters at the two maxima.

## A3 Discarding stations I1 and J3 for $\ell$ Carinae

One of the ATs was positioned at station I1 during run A and at station J3 during run C. Here we remove all baselines involving that telescope to test whether this difference could bias our result. We

Night	01-09	01-10	01-11	02-14	02-15	02-16
$\Theta_{\text{UD}}$ [mas]	3.0979	3.0974	3.0970	3.1118	3.1089	3.1105
$\sigma(\Theta_{\text{UD}})$ [mas]	0.0003	0.0003	0.0003	0.0003	0.0002	0.0003
$\chi_r^2$	2.533	1.763	1.847	3.363	3.204	3.896
$\langle \Theta_{\text{UD}} \rangle$ [mas]	$3.0974 \pm 0.0002$			$3.1104 \pm 0.0006$		
$\Delta \langle \Theta_{\text{UD}} \rangle$ [mas]	$0.013 \pm 0.001$					

**Table A1.** Uniform disk diameters determined for nights near maximum with short baseline removed. The three-night averages are nearly identical to the results in Tab. 5 and indicate a larger second maximum.

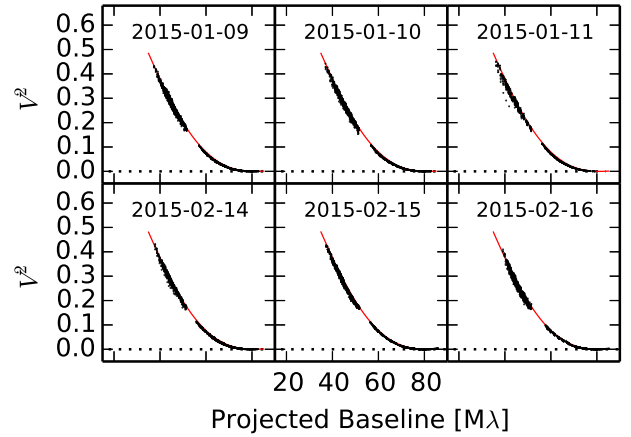


**Figure A2.** Visibility curves with short baselines removed for nights near maximum diameter.

Night	01-09	01-10	01-11	02-14	02-15	02-16
$\Theta_{\text{UD}}$ [mas]	3.0999	3.0978	3.0976	3.1066	3.1080	3.1106
$\sigma(\Theta_{\text{UD}})$ [mas]	0.0004	0.0003	0.0004	0.0003	0.0002	0.0003
$\chi_r^2$	2.603	1.868	2.152	1.853	2.623	3.140
$\langle \Theta_{\text{UD}} \rangle$ [mas]	$3.0985 \pm 0.0006$			$3.1084 \pm 0.0010$		
$\Delta \langle \Theta_{\text{UD}} \rangle$ [mas]	$0.010 \pm 0.001$					

**Table A2.** Uniform disk diameters determined for nights near maximum with all I1 (run A) and J3 (run C) baselines removed. The three-night averages show a clear difference, indicating a larger second maximum.

show the resulting  $V^2$  curves in Fig. A3 and list the UD diameters in Tab. A2. The resulting diameters are in agreement with the results including all baselines, and the difference between the maximal diameters remains clear.

## A4 Closure phase stability

Figures A5 through A7 present the stability of closure phases for all calibrator stars. To within the precision of *PIONIER*, none of the calibrator/standard stars shows signs of asymmetry or companions (known binaries were rejected by Lafrasse et al. 2010, and none of the calibrators are listed as multiples in Mérand et al. 2005). The absence of time-dependent changes suggests that the changing azimuthal angle of the observations does not introduce a bias for the diameter determination.

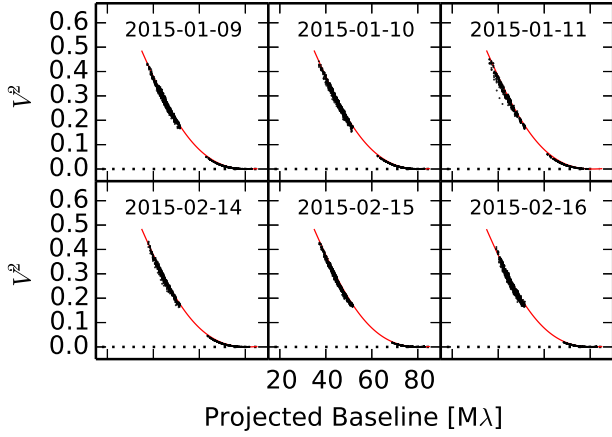


**Figure A3.** Visibility curves with baselines I1 (run A) and J3 (run C) removed for nights near maximum diameter.

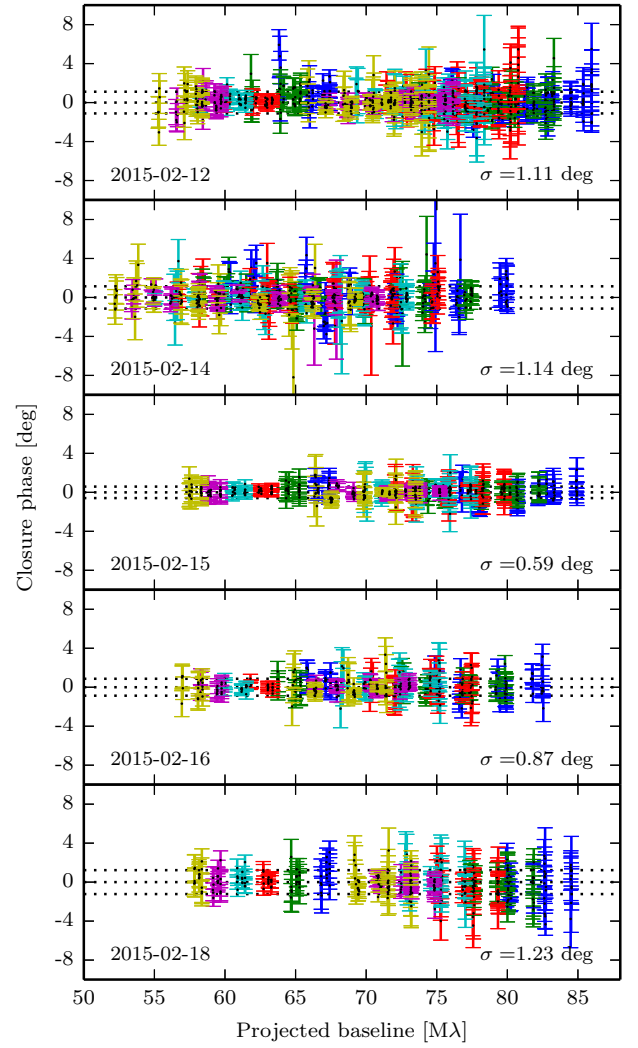


**Figure A4.** Closure phases versus projected baseline for standard star HD 74088. All panels have identical axis ranges. The dotted lines indicate 0 degrees and the  $1\sigma$  range, which is also given in the bottom right of each panel. The night of observation is printed in the bottom left of each panel. Different colors represent different spectral channels.

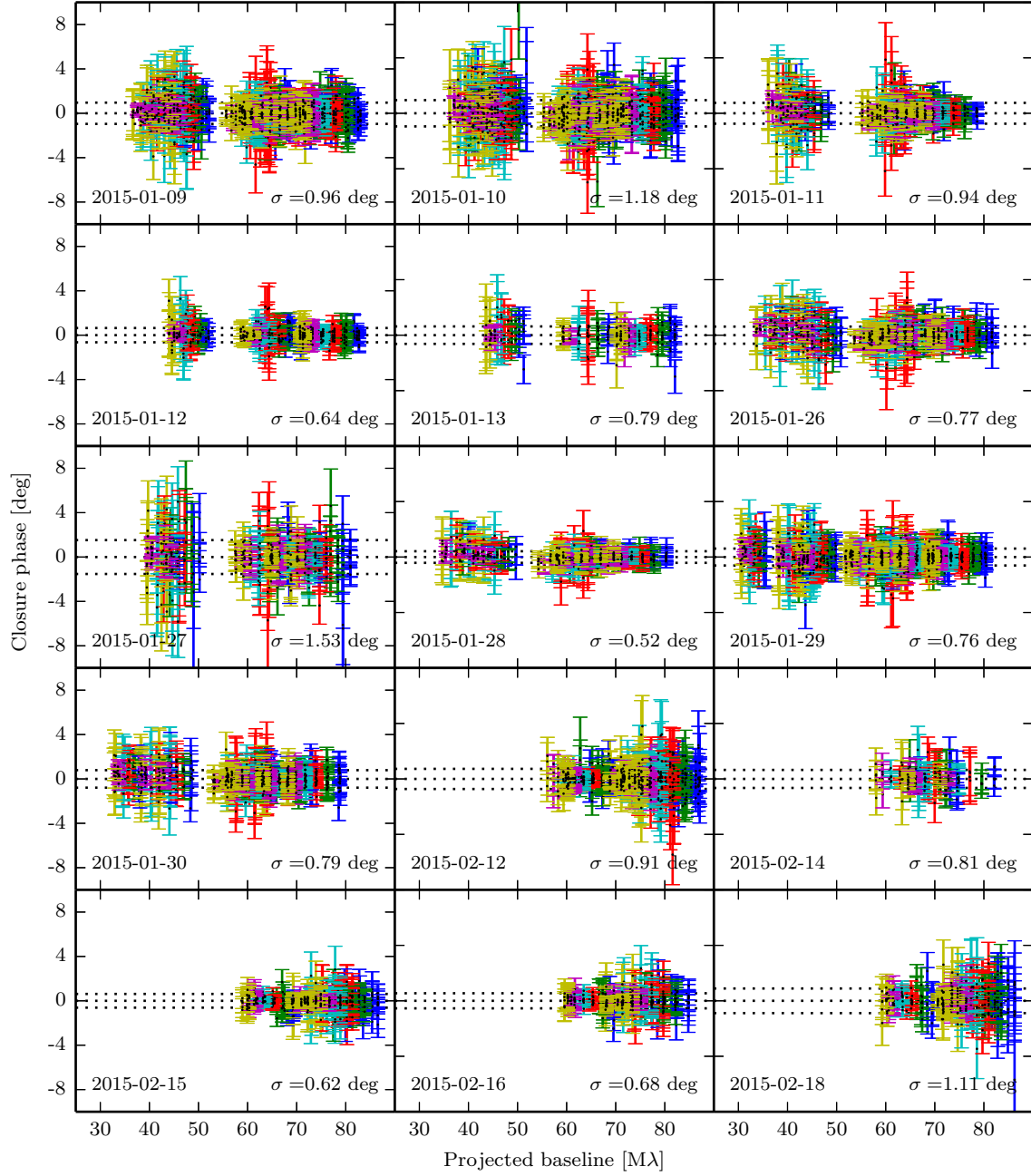


**Figure A5.** Closure phases versus projected baseline for calibrator star HD 81502, cf. also Fig. A4.

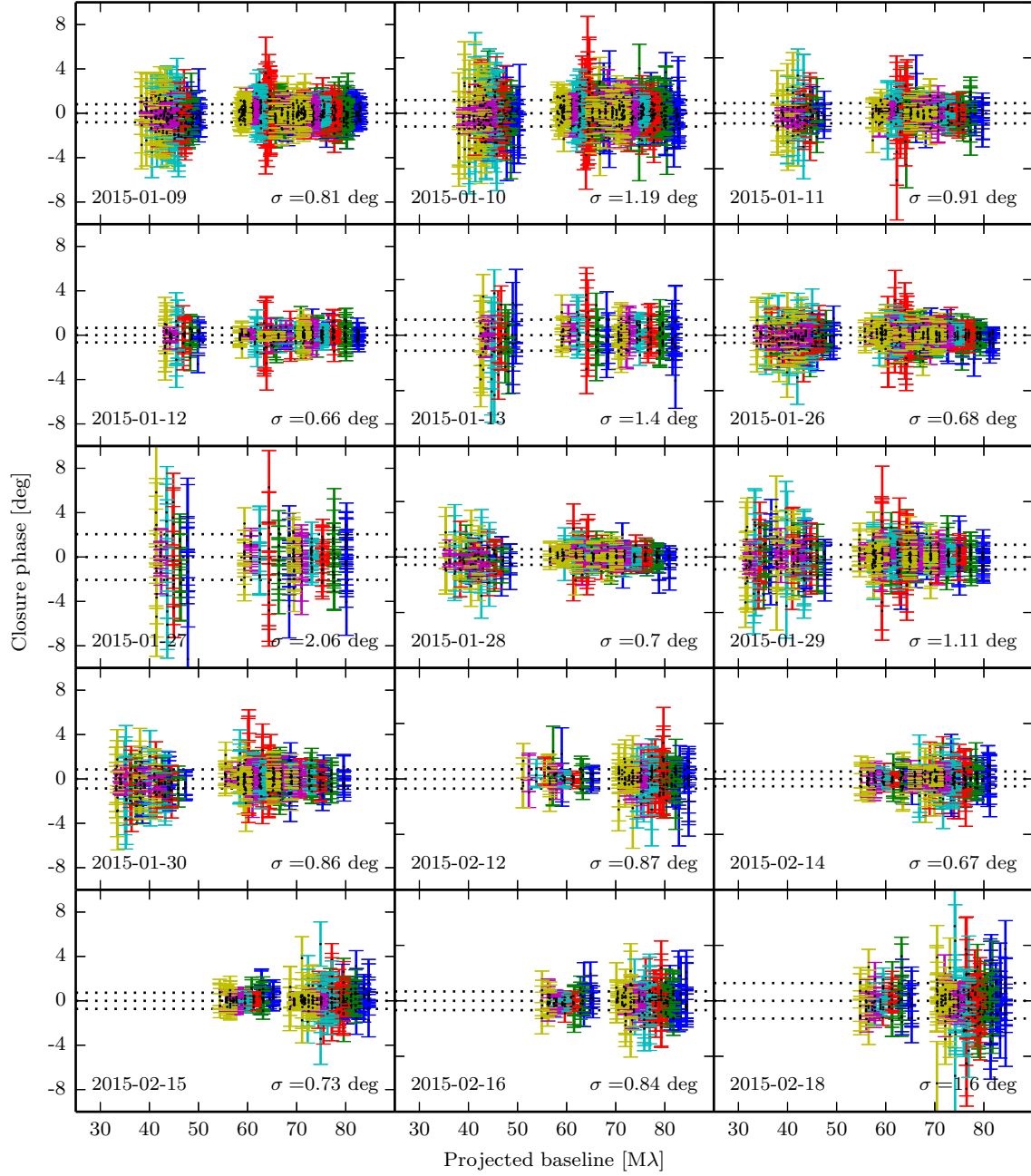


**Figure A6.** Closure phases versus projected baseline for calibrator star HD 89805, cf. also Fig. A4.

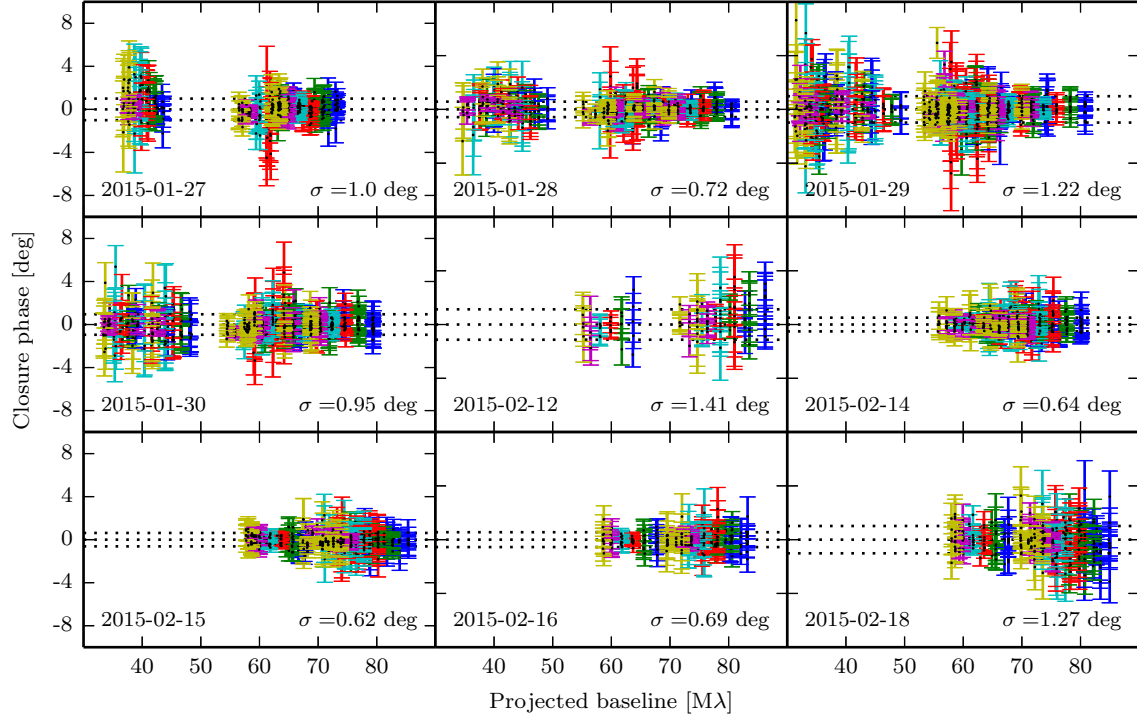


**Figure A7.** Closure phases versus projected baseline for standard star HD 81101, cf. also Fig. A4.